Centrifuging of Hydrometeors and Debris in Tornadoes: Radar-Reflectivity Patterns and Wind-Measurement Errors

DAVID C. DOWELL

Advanced Study Program, National Center for Atmospheric Research, Boulder, Colorado*

CURTIS R. ALEXANDER

School of Meteorology, University of Oklahoma, Norman, Oklahoma

JOSHUA M. WURMAN

Center for Severe Weather Research, Boulder, Colorado

LOUIS J. WICKER

National Severe Storms Laboratory, Norman, Oklahoma

(Manuscript received 21 November 2003, in final form 27 October 2004)

ABSTRACT

High-resolution Doppler radar observations of tornadoes reveal a distinctive tornado-scale signature with the following properties: a reflectivity minimum aloft inside the tornado core (described previously as an "eye"), a high-reflectivity tube aloft that is slightly wider than the tornado core, and a tapering of this high-reflectivity tube near the ground. The results of simple one-dimensional and two-dimensional models demonstrate how these characteristics develop. Important processes in the models include centrifugal ejection of hydrometeors and/or debris by the rotating flow and recycling of some objects by the near-surface inflow and updraft.

Doppler radars sample the motion of objects within the tornado rather than the actual airflow. Since objects move at different speeds and along different trajectories than the air, error is introduced into kinematic analyses of tornadoes based on radar observations. In a steady, axisymmetric tornado, objects move outward relative to the air and move more slowly than the air in the tangential direction; in addition, the vertical air-relative speed of an object is less than it is in still air. The differences between air motion and object motion are greater for objects with greater characteristic fall speeds (i.e., larger, denser objects) and can have magnitudes of tens of meters per second. Estimates of these differences for specified object and tornado characteristics can be obtained from an approximation of the one-dimensional model.

Doppler On Wheels observations of the 30 May 1998 Spencer, South Dakota, tornado demonstrate how the apparent tornado structure can change when the radar-scatterer type changes. When the Spencer tornado entered the town and started lofting debris, changes occurred in the Doppler velocity and reflectivity fields that are consistent with an increase in mean scatterer size.

1. Introduction

Radar scans at close ranges to tornadoes, especially those obtained recently with mobile ground-based radars (e.g., Fig. 1), have revealed a distinctive tornadic signature. This tornado-scale (~1 km wide, ~10 km deep) signature has the following properties:

1) The tornado core (i.e., the region inside the radius of maximum tangential wind) and its immediate surroundings are associated with a minimum in reflectivity, described previously as an "eye" (Fujita 1981; Wurman et al. 1996; Wakimoto et al. 1996; Wurman and Gill 2000; Bluestein and Pazmany 2000).
2) Aloft, a high-reflectivity tube outside the tornado core surrounds the reflectivity minimum (Bluestein et al.

* The National Center for Atmospheric Research is sponsored by the National Science Foundation.

Corresponding author address: David C. Dowell, Cooperative Institute for Mesoscale Meteorological Studies, 1313 Halley Circle, Norman, OK 73069.
E-mail: David.Dowell@noaa.gov

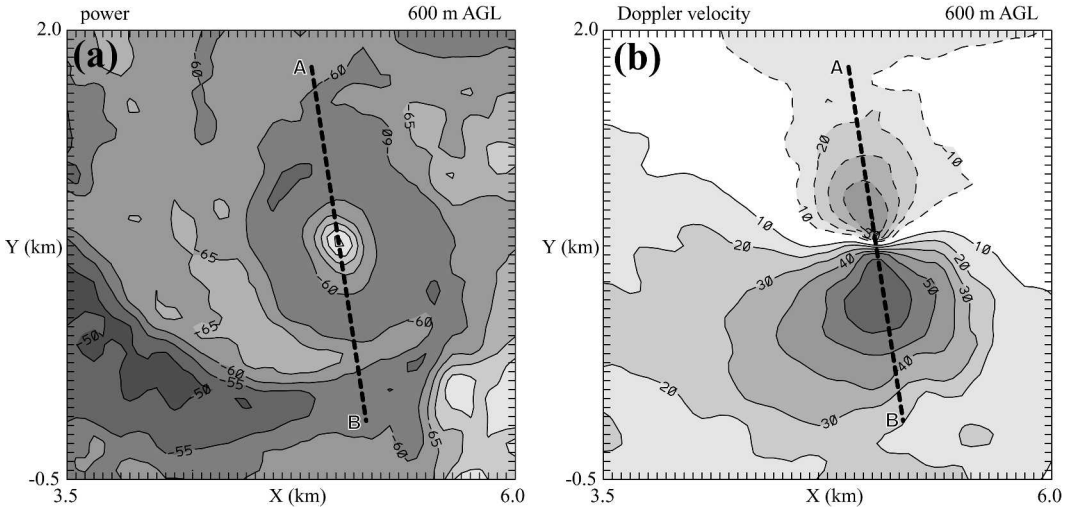

FIG. 1. Objectively analyzed received power (contouring and shading at intervals of 5 dBm) and Doppler velocity (contouring and shading at intervals of 10 m s^{-1}; negative values indicated by dashed lines) in the Spencer, SD, tornado at 0140 UTC 31 May 1998. Horizontal distances (km) are relative to the radar (DOW3). (a) Received power at 600 m AGL in a 2.5 km × 2.5 km region. (b) As in (a) except for Doppler velocity. (c) Received power in a 2-km-long vertical cross section (indicated by the dashed line in previous panels). At the center of the tornado, the cross section is perpendicular to the radar beams. (d) As in (c), except for Doppler velocity. (e) Vertical cross section of received power superimposed on a video image (copyright D. Dowell) of the Spencer tornado taken from the radar site at 0140:05 UTC. (f) As in (e), except for Doppler velocity.

1993; Wurman et al. 1996; Wurman and Gill 2000; Wurman and Samaras 2004; Bluestein et al. 2004b).

3) The high-reflectivity tube is tapered at the bottom; the tornado is often associated with relatively high reflectivity near the ground (Wurman et al. 1996; Wurman and Gill 2000; Wurman and Samaras 2004; Bluestein et al. 2004b).
4) Strong radial flow into the tornado (i.e., horizontal convergence of the same magnitude as the vertical vorticity) that would be expected near the surface (Hoecker 1960; Golden and Purcell 1977; Lewellen 1993) is usually not indicated by radar measurements (Wurman et al. 1996; Wurman and Gill 2000; Bluestein et al. 2003).

The tornado-scale reflectivity feature is typically attached to a storm-scale hook echo (Stout and Huff 1953; van Tassell 1955). Horizontal radar sweeps through some tornadoes reveal multiple concentric reflectivity annuli, particularly within a few hundred meters of the ground (Wurman and Gill 2000). Reflectivity eyes have also been observed in other types of vortices, such as dust devils (Bluestein et al. 2004a) and subvortices within tornadoes (Wurman 2002). Reflectivity protrusions into the eye (Wurman et al. 1996) and fluctuations in the width of the high-reflectivity tube (Wurman and Gill 2000) have been observed but are beyond the scope of this study.

Detailed observations of tornadoes have been collected with both centimeter-wavelength (Wurman and Gill 2000) and millimeter-wavelength radars (Bluestein and Pazmany 2000). Significant radar scatterers in high-reflectivity regions could include hydrometeors, insects, gravel, plant material, and debris from man-made structures; in the case of millimeter-wavelength radar observations, smaller scatterers might also be significant (Bluestein and Pazmany 2000). In our study, we assume the scatterers are debris (with relatively large fall speeds) and hydrometeors, but the conclusions drawn from this study are easily applicable to other scatterer types.

The pressure-gradient force that accelerates air inward in vortex flow is too weak to have much impact on the trajectories of relatively dense particles within the vortex. Therefore, dense particles in the vortex move outward relative to the air; that is, they are "centrifuged" (Snow 1984). Several decades ago, Kangieser (1954) hypothesized that the visual hollowness of tornadoes resulted from centrifuging of water droplets. More recently, references in the literature to centrifuging of hydrometeors and debris in tornadoes have increased as more and more detailed radar observations have been collected (Zrnic et al. 1977, 1985; Wakimoto and Martner 1992; Bluestein et al. 1993; Wurman et al. 1996; Wurman and Gill 2000; Dowell and Bluestein 2002; Burgess et al. 2002). Observations 1 and 2 above,

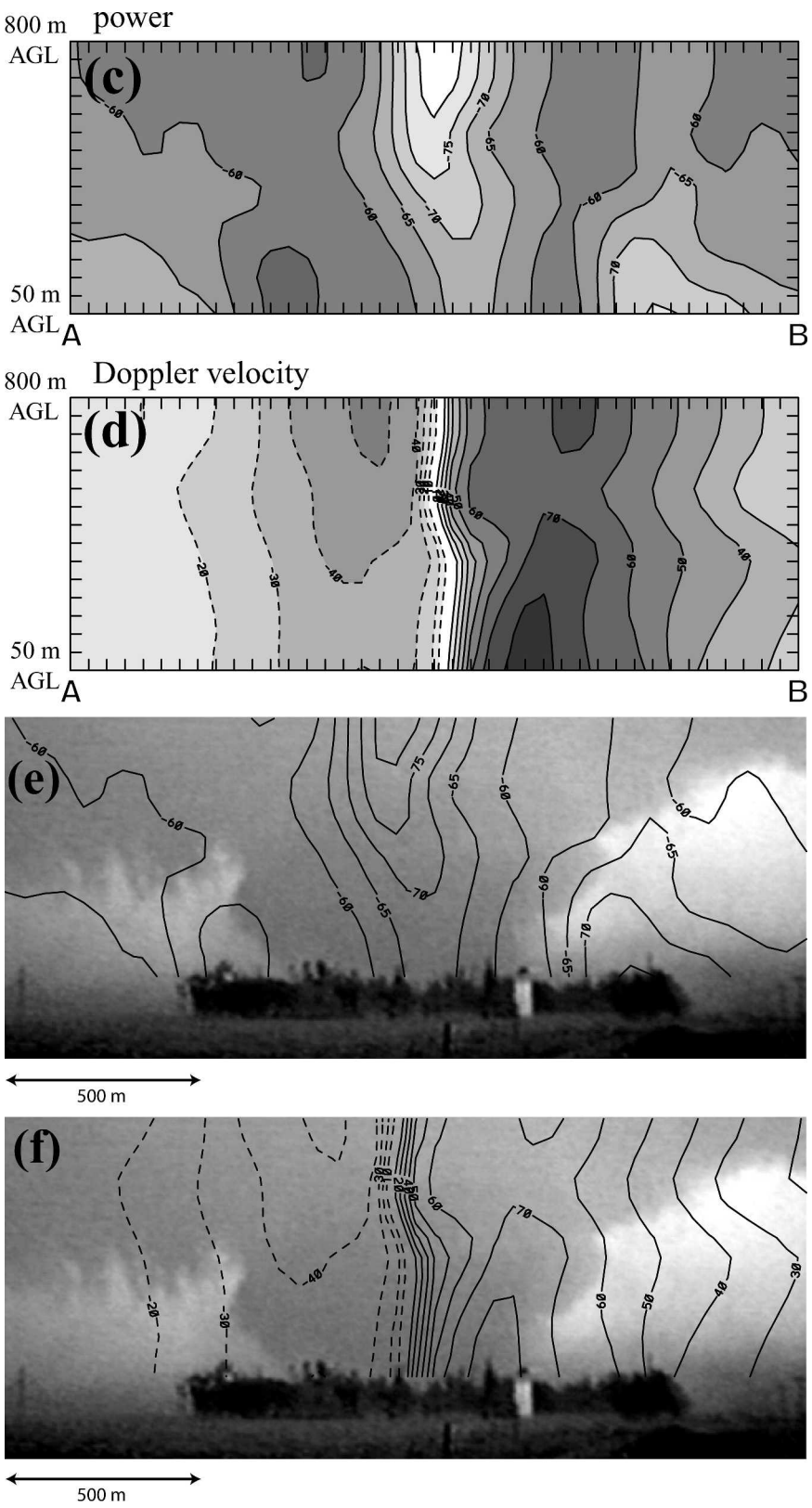

FIG. 1. (*Continued*)

and observation 4 to some degree, have been attributed to centrifuging.

Here we more thoroughly investigate mechanisms for producing the observed reflectivity and velocity patterns in tornadoes and describe the implications of this work for kinematic analyses of radar observations of tornadoes. We particularly emphasize the difference between the Doppler velocity, which represents the motion of the objects that scatter energy back to the radar, and the air velocity. For the purposes of kinematic analysis, this difference is part of the "measurement error." Using idealized one-dimensional (1D; section 2) and two-dimensional (2D; section 3) models, we quantify for typical tornadoes the measurement error associated with incorrectly equating Doppler velocity to air velocity. Then, in section 4, we relate the results of the numerical experiments to high-resolution Doppler measurements of a violent tornado. We close with suggestions for future work.

2. One-dimensional model

Following Snow (1984), we consider how a field of particles/objects responds to a specified vortex airflow, which is assumed to be steady. Although hydrometeors and other objects could affect the airflow in real vortices (Eskridge and Das 1976; Davies-Jones 2000), we do not consider such effects here. Subgrid-scale processes such as coalescence of hydrometeors are also neglected. Here, the vortex is assumed to be symmetric about a vertical axis and vertically uniform. The equations governing the motion and number concentration of particles/objects within such a vortex are as follows:

$$\frac{\partial u_p}{\partial t} = -u_p \frac{\partial u_p}{\partial r} + \frac{v_p^2}{r} - \frac{1}{\rho_p}\frac{\partial p}{\partial r} + F_u, \tag{1}$$

$$\frac{\partial v_p}{\partial t} = -u_p \frac{\partial v_p}{\partial r} - \frac{u_p v_p}{r} + F_v, \tag{2}$$

$$\frac{\partial w_p}{\partial t} = -u_p \frac{\partial w_p}{\partial r} - g + F_w, \quad \text{and} \tag{3}$$

$$\frac{\partial n}{\partial t} = -\frac{1}{r}\frac{\partial}{\partial r}(nru_p), \tag{4}$$

where r is the distance from the vortex center; t is time; $u_p(r, t)$, $v_p(r, t)$, and $w_p(r, t)$ are the radial, tangential, and vertical velocity components, respectively, of the objects; $n(r, t)$ is the number concentration of objects; ρ_p is the density of the objects; $p(r)$ is the air pressure; and $F_u(r, t)$, $F_v(r, t)$, and $F_w(r, t)$ are the drag forces per unit mass exerted on the objects by the air in the radial, tangential, and vertical directions, respectively. Our model is similar to Snow's (1984), except that we solve for all three velocity components, rather than just the radial component. Snow considered dust particles, which are so small that the air and particle tangential velocities are virtually the same. As demonstrated later, the tangential velocities of the larger objects in our model instead differ significantly from those of the air.

TABLE 1. Approximate terminal fall speeds $|w_t|$ of hydrometeors and debris in an atmosphere of density 1.2 kg m^{-3}.

Object	Fall speed
Small raindrop (0.5-mm diameter)	2 m s^{-1} (Gunn and Kinzer 1949)
Large raindrop (5-mm diameter)	9 m s^{-1} (Gunn and Kinzer 1949)
Small hailstone (1-cm diameter)	10 m s^{-1} (Matson and Huggins 1980)
Large hailstone (5-cm diameter)	25 m s^{-1} (Matson and Huggins 1980)
Personal check: dry, wet	0.5, 1.5 m s^{-1} (Magsig and Snow 1998)
Plywood sheet, tumbling	20 m s^{-1} (Hoecker 1960)
Brick	40 m s^{-1} (estimated from study by Minor et al. 1977)

The drag coefficient in standard expressions for the drag force depends not only on an object's size and shape but also on the object-relative airspeed and the degree of environmental turbulence (Stackpole 1961; Bohne 1982). Our primary interest here is to compare the motions of objects that differ greatly in size and shape. Since the dependence of the drag coefficient on turbulence and object-relative airspeed is expected to be of secondary importance, we employ the simplifying assumption that an individual object's drag coefficient is constant and equal to the value attained when the object is falling at its terminal fall velocity (hereafter, w_t) through still air (Stackpole 1961; Bohne 1982). From the work of Gunn and Kinzer (1949) and Matson and Huggins (1980), we estimate that the errors in this assumption are ~10% for our simulations.

Terminal fall speeds of various objects are readily available (e.g., Table 1). Characterizing an object's drag properties in terms of w_t results in the following compact expressions for the drag terms in (1)–(3):

$$F_u = \frac{g(u_a - u_p)|\mathbf{v}_a - \mathbf{v}_p|}{w_t^2}, \tag{5}$$

$$F_v = \frac{g(v_a - v_p)|\mathbf{v}_a - \mathbf{v}_p|}{w_t^2}, \tag{6}$$

$$F_w = \frac{g(w_a - w_p)|\mathbf{v}_a - \mathbf{v}_p|}{w_t^2}, \tag{7}$$

where g is the gravitational acceleration; $u_a(r)$, $v_a(r)$, and $w_a(r)$ are the radial, tangential, and vertical velocity components, respectively, of the air; $\mathbf{v}_a(r)$ is the air-velocity vector; and $\mathbf{v}_p(r, t)$ is the object-velocity vector.

To derive (5)–(7), we assumed the drag coefficient was the same in the horizontal as in the vertical. This assumption should be valid for small raindrops, which remain approximately spherical (e.g., Pruppacher and Beard 1970). To justify this assumption for large, oblate raindrops, we must assume that drops remain flattened in the direction of the drag force.[1] Solid, irregularly shaped objects such as hail and debris generally tumble when they fall (e.g., Hoecker 1960; Matson and Huggins 1980). Tumbling about a horizontal axis results in a mean cross-sectional area, and therefore a drag coefficient, that is the same in one horizontal direction as it is in the vertical. Our assumption of an isotropic drag coefficient is applicable to a field of objects in which the orientations of the tumbling are random.

A scale analysis indicates that the pressure-gradient term in (1) can be neglected if the objects are relatively dense. For example, in a cyclostrophically balanced vortex,

$$\frac{v_a^2}{r} = \frac{1}{\rho_a}\frac{\partial p}{\partial r}, \tag{8}$$

where ρ_a is the air density. If we assume $|v_a| \sim |v_p|$, then the ratio of the pressure-gradient term to the curvature term in (1) is as follows:

$$\frac{\left|\frac{1}{\rho_p}\frac{\partial p}{\partial r}\right|}{\left|\frac{v_p^2}{r}\right|} \sim \frac{\left|\frac{1}{\rho_p}\frac{\partial p}{\partial r}\right|}{\left|\frac{v_a^2}{r}\right|} = \frac{\left|\frac{1}{\rho_p}\frac{\partial p}{\partial r}\right|}{\left|\frac{1}{\rho_a}\frac{\partial p}{\partial r}\right|} = \frac{\rho_a}{\rho_p}. \tag{9}$$

For the object types we are considering (e.g., raindrops: $\rho_p = 1000\ \text{kg m}^{-3}$), the ratio in (9) is ~0.001. Therefore, the pressure-gradient term is relatively small and can be neglected.

We solved Eqs. (1)–(7) for two types of idealized vortices:

$$\text{Rankine vortex} \quad u_a = 0; \quad w_a = 0; \quad v_a = \frac{Vr}{R}, \quad r \le R;$$
$$v_a = \frac{VR}{r}, \quad r \ge R; \tag{10}$$

$$\text{Fiedler vortex} \quad u_a = 0; \quad w_a = 0; \quad v_a = \frac{2VRr}{R^2 + r^2}, \tag{11}$$

where R is the radius of the vortex core, and V is the tangential velocity at the edge of the core. The Rankine combined vortex defined by (10) is perhaps the simplest and most popular tornado model. The vortex defined by (11) is of a form described by Fiedler [1989, Eq. (3.18)], except we are not considering the radial and vertical motions that Fiedler included in his solution. The tangential velocity profile in the Fiedler vortex is perhaps more physical because there is no cusp (i.e., no discontinuity in $\partial v_a/\partial r$) like that at the edge of a Rankine vortex core. These idealized profiles, in which $u_a = 0$, are most applicable to the portion of a tornado above the surface layer, where radial motions are relatively weak (Snow 1984). For simplicity, we assume $w_a = 0$ in the 1D experiments; thus, the total object-relative airspeed is $|\mathbf{v}_a - \mathbf{v}_p| = \sqrt{u_p^2 + (v_a - v_p)^2 + w_p^2}$. The roles of radial and vertical air motions will be considered later in the experiments with the 2D model.

We simulated the motion of the following objects: small raindrops ($|w_t| = 2\ \text{m s}^{-1}$), large raindrops/small hailstones ($|w_t| = 10\ \text{m s}^{-1}$), large hailstones/plywood sheets ($|w_t| = 20\ \text{m s}^{-1}$), and bricks ($|w_t| = 40\ \text{m s}^{-1}$) (Table 1). The fall speed of a brick is somewhat speculative but is intended to represent a large, dense piece of debris. At the initial time ($t = 0$ s) in the simulations, we assumed the objects were moving at the same horizontal velocities as the air and that they were falling at their terminal fall speeds. The quantity $\tau = (w_t^2/g|\mathbf{v}_a - \mathbf{v}_p|)$, the inverse of which appears in (5)–(7), is a relaxation time scale for how quickly objects respond to the drag force (Stackpole 1961). For the specified initialization and object types, $\tau = (w_t^2/g|w_t|) = 0.2$ to 4.1 s; therefore, after a few tens of seconds, the object motions are determined by the forcing (the wind profile and gravity) rather than by the initialization. The results shown in Figs. 2–4 and Table 2 are at $t = 100$ s, by which time the profiles of object motion have asymptotically approached steady solutions. Other choices for the initialization (e.g., $u_p = v_p = w_p = 0$) produce results at $t = 100$ s that are indistinguishable from those in Figs. 2 and 3.

The first simulations of object motions were for vortices with $V = 100\ \text{m s}^{-1}$ at $R = 100$ m (Figs. 2 and 3). Objects of increasing characteristic fall speeds move at increasingly slower tangential speeds (Figs. 2a and 3a). Near the radius of maximum tangential wind, small raindrops have tangential speeds within $1\ \text{m s}^{-1}$ of the airspeed, whereas larger objects move a few tens of meters per second more slowly than the air. The results

[1] The minor axes of large drops falling through still air are vertical (Pruppacher and Beard 1970). We speculate that drops that are both falling and being centrifuged outward have nonvertical minor axes. Differences in drop orientation associated with centrifuging would be detectable with dual-polarization radar.

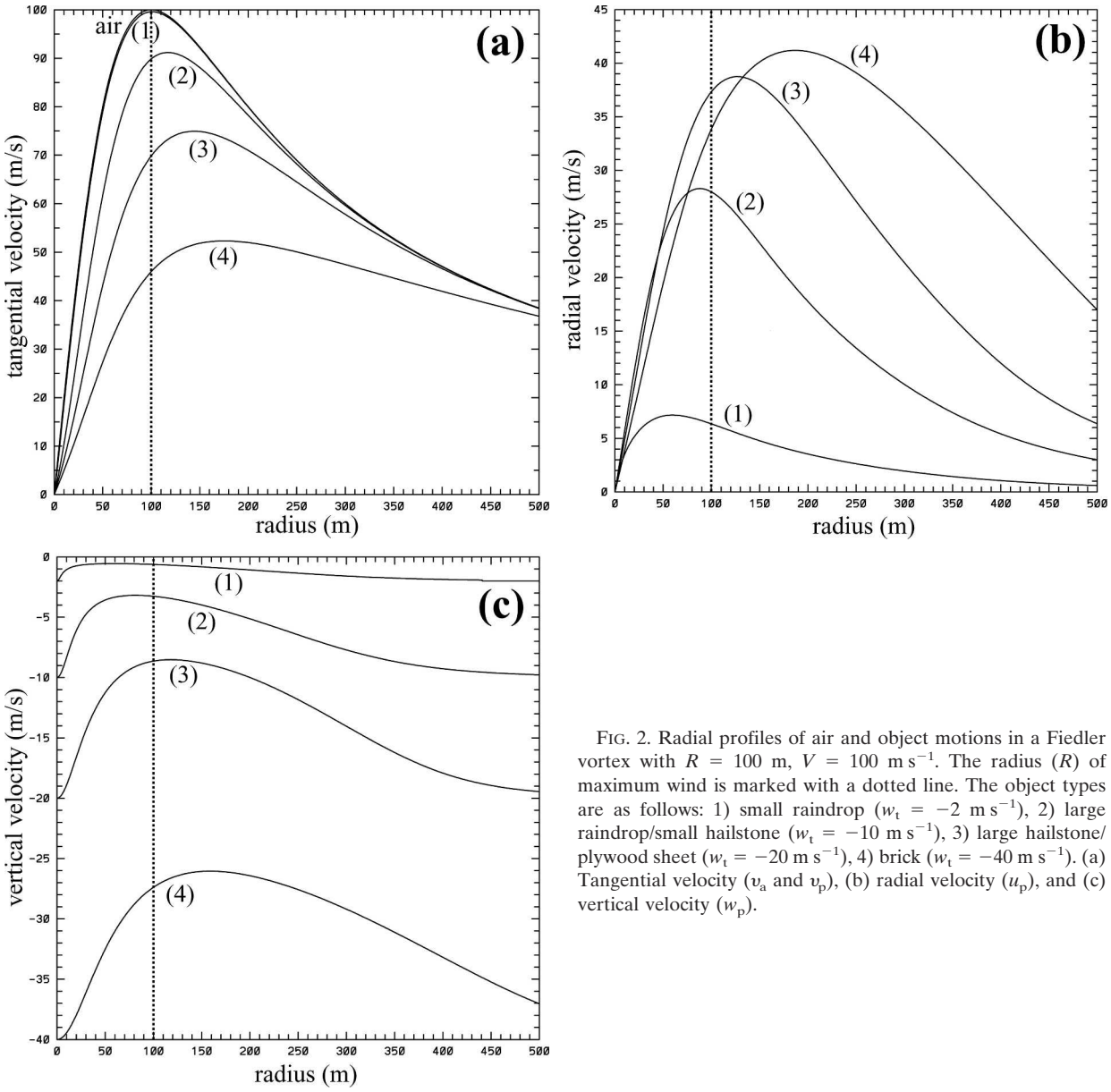

FIG. 2. Radial profiles of air and object motions in a Fiedler vortex with $R = 100$ m, $V = 100$ m s^{-1}. The radius (R) of maximum wind is marked with a dotted line. The object types are as follows: 1) small raindrop ($w_t = -2$ m s^{-1}), 2) large raindrop/small hailstone ($w_t = -10$ m s^{-1}), 3) large hailstone/plywood sheet ($w_t = -20$ m s^{-1}), 4) brick ($w_t = -40$ m s^{-1}). (a) Tangential velocity (v_a and v_p), (b) radial velocity (u_p), and (c) vertical velocity (w_p).

are somewhat sensitive to the vortex profile. For example, in the Rankine vortex, which has a cusp in the velocity profile, large hailstones reach a maximum tangential speed of 68 m s^{-1} (Fig. 3a; Table 2, row 2). In the Fiedler vortex, the large hailstones move at tangential speeds of up to 75 m s^{-1} (Fig. 2a; Table 2, row 1). In both vortex types, the maxima in tangential velocities of the objects occur just outside the peak in tangential air velocity.

In these simulations, objects move outward at significant speeds (Figs. 2b and 3b; Table 2). When $V = 100$ m s^{-1} and $R = 100$ m, small raindrops move outward with respect to the air at speeds of over 6 m s^{-1}, and the larger objects move outward at 25 to 41 m s^{-1}. The peaks in outward motion occur at increasingly larger radii for increasing $|w_t|$. The results are again somewhat sensitive to the nature of the vortex. In the Fiedler vortex, some of the peaks in u_p occur inside the radius of maximum tangential wind, whereas in the Rankine vortex, all of the peaks in u_p occur outside the radius of maximum wind. The maximum radial speeds of objects in the Rankine vortex are 1–5 m s^{-1} less than those in the Fiedler vortex.

An object that is both falling and being centrifuged experiences a total relative airspeed that is greater than when it is falling through still air. For example, at $r =$

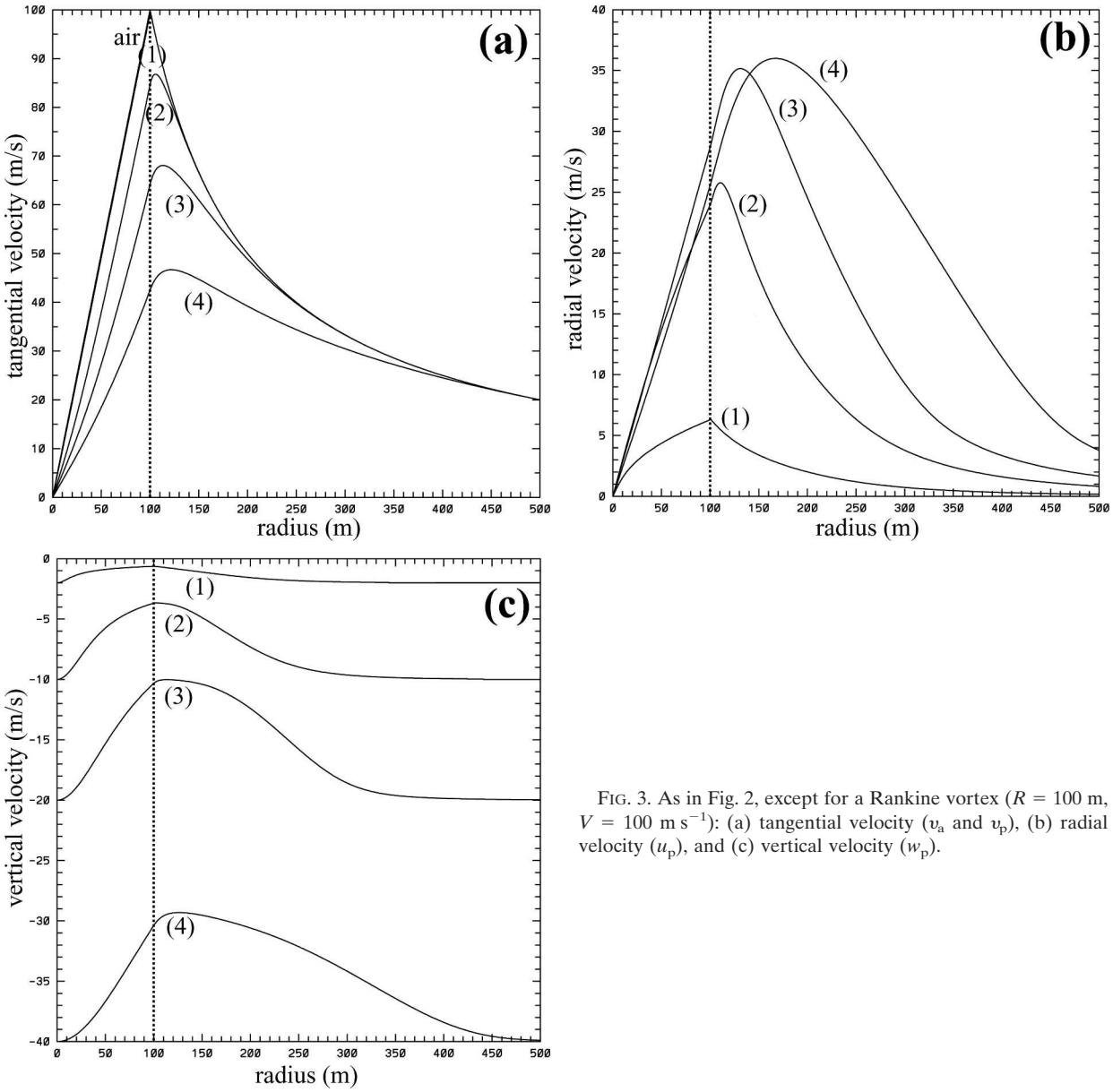

FIG. 3. As in Fig. 2, except for a Rankine vortex (R = 100 m, V = 100 m s^{-1}): (a) tangential velocity (v_a and v_p), (b) radial velocity (u_p), and (c) vertical velocity (w_p).

110 m in the Rankine vortex (Table 2, row 2), the airspeed with respect to a large raindrop is $|\mathbf{v}_a - \mathbf{v}_p| = 29.2$ m s^{-1}, whereas $|\mathbf{v}_a - \mathbf{v}_p| = |w_t| = 10.0$ m s^{-1} in still air. Owing to the centrifuged object's greater relative airspeed, the balance between gravity and the vertical component of the drag force is achieved at $|w_a - w_p| < |w_t|$ [cf. Eqs. (3) and (7)]. Thus, a conclusion from the 1D simulations is that objects fall more slowly within vortices than in still air (Figs. 2c and 3c). In the Rankine vortex (Fig. 2c), the fall speeds of the small raindrops, large raindrops, large hailstones, and bricks are reduced by as much as 70%, 63%, 50%, and 27%, respectively. The ratios between w_p and u_p (Table 2) indicate that objects, particularly those with $|w_t| \leq 20$ m s^{-1}, are ejected from the vortex core at relatively small angles with respect to the horizontal. The quasi-horizontal object trajectories in these simulations could help explain why some debris falls out farther outside the tornado core than might be expected (e.g., Marshall 2002). Anomalous motion associated with object rotation (Martin 1998) is probably another important factor in explaining the trajectories of debris projectiles.

We now consider object motions in vortices of different intensities and sizes. Fiedler and Rankine vortices of the same radius described previously (R = 100 m) but half the maximum wind speed (V = 50 m s^{-1})

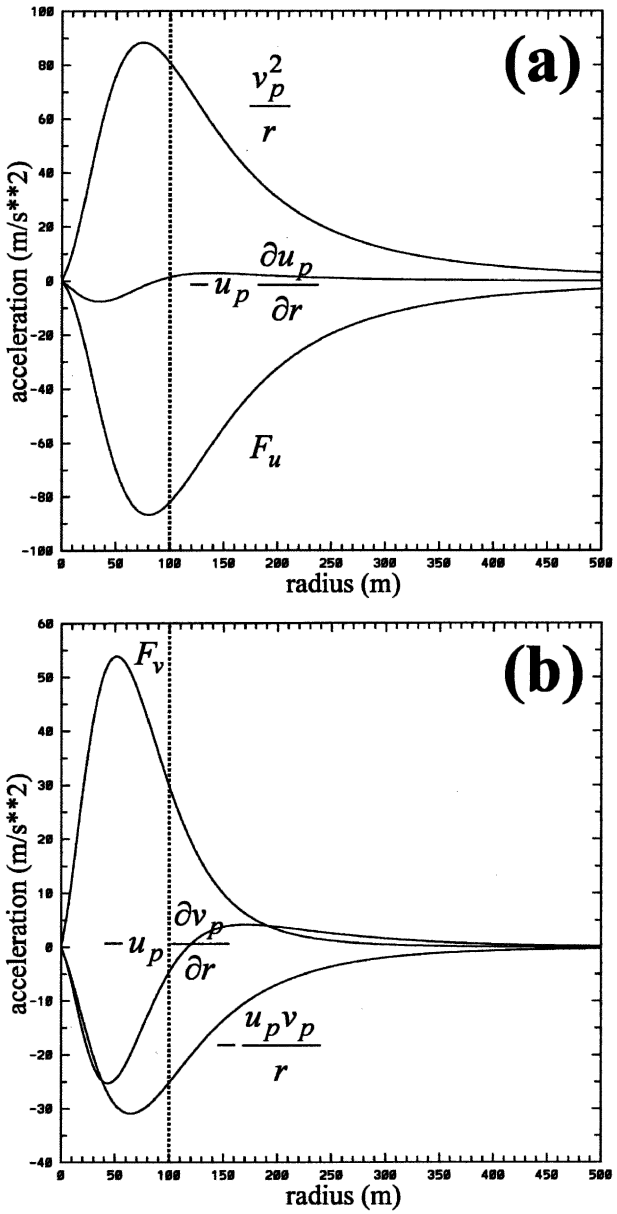

FIG. 4. Radial profiles of the terms in the equations of motion for the vortex shown in Fig. 2. In this example, the hydrometeors are large raindrops/small hailstones ($w_t = -10$ m s^{-1}). (a) Forcing in the u_p equation; (b) forcing in the v_p equation.

are associated with object-motion profiles (not shown) of similar shape to those in Figs. 2 and 3. The magnitudes of u_p and v_p in the vortices with $V = 50$ m s^{-1} (Table 2, rows 3–4) are approximately half those in the vortices with $V = 100$ m s^{-1} (Table 2, rows 1–2).

In another experiment, we doubled the radius of maximum wind from $R = 100$ m to $R = 200$ m while keeping $V = 100$ m s^{-1} (Table 2, rows 1–2 and 5–6). The objects reach higher tangential speeds in the wider vortex than in the narrower vortex. For example, in Rankine vortices with $V = 100$ m s^{-1}, the large hailstones achieve a maximum tangential speed of 79 m s^{-1} in the wider vortex but only 68 m s^{-1} in the narrower one. In addition, slower radial object motion occurs in the wider vortex; the objects in the wider vortex move outward at peak speeds that are 2–6 m s^{-1} less than those in the narrower vortex.

Rather than using a full time-dependent 1D model, one might desire a quicker method for estimating the measurement error associated with centrifuging for a particular tornado and scatterer type. From approximations to (1)–(3), one can estimate the maxima in u_p, v_p, and w_p in the idealized vortices. First, since we are interested here in the steady-state solutions for the object motions, we neglect the local time derivatives in (1)–(3). Second, we neglect the advection terms because they are zero at the maxima in u_p, v_p, and w_p. Thus, the approximate balance of remaining forces is between the curvature terms, drag, and gravity:

$$-\frac{v_p^2}{r} \approx \frac{g(u_a - u_p)|\mathbf{v}_a - \mathbf{v}_p|}{w_t^2}, \tag{12}$$

$$\frac{u_p v_p}{r} \approx \frac{g(v_a - v_p)|\mathbf{v}_a - \mathbf{v}_p|}{w_t^2}, \tag{13}$$

$$g \approx \frac{g(w_a - w_p)|\mathbf{v}_a - \mathbf{v}_p|}{w_t^2}. \tag{14}$$

Third, we employ an approximation that the maxima in u_p, v_p, and w_p all occur at the radius of maximum wind. Although the true profiles are more complicated (Figs. 2 and 3), the radius of maximum wind is a reasonable guess for where the maxima occur. Furthermore, at the radius of maximum wind, the advection terms are much smaller than the curvature and drag terms (Fig. 4); thus, our second assumption is still reasonable.

For example, to estimate the maxima in u_p, v_p, and w_p, one can solve (12)–(14) iteratively after making the following substitutions: $u_a = 0$, $v_a = V$, and $r = R$. Table 3 summarizes the solutions to the approximate Eqs. (12)–(14) for vortices of all widths and strengths described previously (Table 2). All estimated maxima in the object-velocity components are within 0.9, 4.4, 8.5, and 14.0 m s^{-1} of the true maxima for the small raindrops, large raindrops, large hailstones, and bricks, respectively.

In simulations of object number concentrations, we specified uniform initial distributions ($n = 1.0$ at $t = 0$ s; Fig. 5). Since we are interested in only relative magnitudes, we did not assign dimensions to the number concentration. In the model, centrifuging of objects quickly produces a minimum in number concentration within the vortex core and a surrounding annulus of

TABLE 2. Maximum radial (u_p), tangential (v_p), and vertical (w_p) velocity components of objects within six different vortices. Peak velocities of four object types are shown: small raindrops ($|w_t| = 2$ m s^{-1}), large raindrops/small hailstones ($|w_t| = 10$ m s^{-1}), large hailstones/plywood sheets ($|w_t| = 20$ m s^{-1}), and bricks ($|w_t| = 40$ m s^{-1}). The radii of the maxima in u_p, v_p, and w_p are indicated in parentheses.

Wind profile	$\lvert w_t \rvert$ (m s^{-1})	Max u_p (m s^{-1})	Max v_p (m s^{-1})	Max w_p (m s^{-1})
1) Fiedler: $R = 100$ m, $V = 100$ m s^{-1} (Fig. 2)	2	7.2 (60 m)	99.6 (100 m)	−0.6 (70 m)
	10	28.3 (90 m)	91.2 (120 m)	−3.2 (80 m)
	20	38.7 (130 m)	74.9 (140 m)	−8.5 (120 m)
	40	41.2 (190 m)	52.3 (180 m)	−26.0 (160 m)
2) Rankine: $R = 100$ m, $V = 100$ m s^{-1} (Fig. 3)	2	6.3 (100 m)	99.3 (100 m)	−0.6 (100 m)
	10	25.8 (110 m)	86.8 (110 m)	−3.7 (110 m)
	20	35.2 (130 m)	68.1 (110 m)	−10.0 (120 m)
	40	36.0 (170 m)	46.7 (120 m)	−29.3 (130 m)
3) Fiedler: $R = 100$ m, $V = 50$ m s^{-1}	2	3.5 (60 m)	49.8 (100 m)	−1.1 (60 m)
	10	13.8 (90 m)	45.9 (120 m)	−6.1 (80 m)
	20	18.9 (120 m)	38.8 (140 m)	−14.7 (100 m)
	40	20.4 (160 m)	29.7 (180 m)	−35.3 (130 m)
4) Rankine: $R = 100$ m, $V = 50$ m s^{-1}	2	3.1 (100 m)	49.7 (100 m)	−1.2 (100 m)
	10	12.4 (110 m)	44.0 (110 m)	−6.8 (100 m)
	20	16.9 (120 m)	35.8 (110 m)	−15.9 (110 m)
	40	17.9 (150 m)	26.8 (120 m)	−36.6 (110 m)
5) Fiedler: $R = 200$ m, $V = 100$ m s^{-1}	2	5.1 (120 m)	99.8 (200 m)	−0.8 (130 m)
	10	22.1 (150 m)	95.4 (220 m)	−4.3 (180 m)
	20	34.0 (210 m)	84.8 (260 m)	−9.9 (190 m)
	40	40.9 (300 m)	65.1 (320 m)	−27.1 (260 m)
6) Rankine: $R = 200$ m, $V = 100$ m s^{-1}	2	4.5 (200 m)	99.7 (200 m)	−0.9 (190 m)
	10	19.9 (210 m)	92.7 (210 m)	−4.7 (200 m)
	20	30.9 (240 m)	79.0 (220 m)	−11.4 (220 m)
	40	36.4 (290 m)	58.8 (240 m)	−30.0 (230 m)

relatively high number concentration (Fig. 5). These characteristics of the distribution are consistent with central minima and surrounding maxima in radar-reflectivity observations of tornadoes. However, the model results so far do not explain all the characteristics of the tornado signature described in the introduction. In observed tornadoes (e.g., Wurman and Gill 2000), the high-reflectivity annulus at a few hundred meters AGL is typically slightly wider than the tornado core, whereas in these 1D simulations, the annulus of high number concentration quickly becomes much wider. For example, after only 60 s in the Rankine vortex illustrated by Fig. 3, the concentrations of small raindrops (Fig. 5), large raindrops (not shown), and small hailstones (not shown) are greatest at radii 2.5, 4.0, and 5.7 times the core radius, respectively. In these 1D simulations, the annulus of high number concentration expands indefinitely without reaching a steady state (Snow 1984). Radial air motions, which will be considered in the following section, are necessary to produce an annulus that does not expand as quickly.

TABLE 3. As in Table 2, except the maximum radial (u_p), tangential (v_p), and vertical (w_p) velocity components are computed from the approximate Eqs. (12)–(14).

Vortex characteristics	$\lvert w_t \rvert$ (m s^{-1})	Max u_p (m s^{-1})	Max v_p (m s^{-1})	Max w_p (m s^{-1})
1) $R = 100$ m, $V = 100$ m s^{-1}	2	6.3	99.6	−0.6
	10	28.4	91.2	−3.3
	20	43.7	74.2	−7.8
	40	50.0	48.0	−21.3
2) $R = 100$ m, $V = 50$ m s^{-1}	2	3.1	49.8	−1.2
	10	13.7	45.9	−6.4
	20	21.2	38.2	−14.2
	40	24.9	27.0	−33.5
3) $R = 200$ m, $V = 100$ m s^{-1}	2	4.5	99.8	−0.9
	10	21.1	95.4	−4.5
	20	36.1	84.6	−9.9
	40	48.4	62.5	−24.3

To summarize the results of the 1D simulations, one should expect significant measurement error when characterizing tornado airflow based on Doppler measurements, particularly if the radar scatterers are large raindrops or even larger targets. The measurement error results in an underestimation of the tangential velocity ($v_p < v_a$) and an overestimation of the radial velocity ($u_p > u_a$). When the scatterers are large raindrops or larger objects, even the weakest tornado considered in this section (Table 2, rows 3–4) would be associated with measurement errors that are an order of magni-

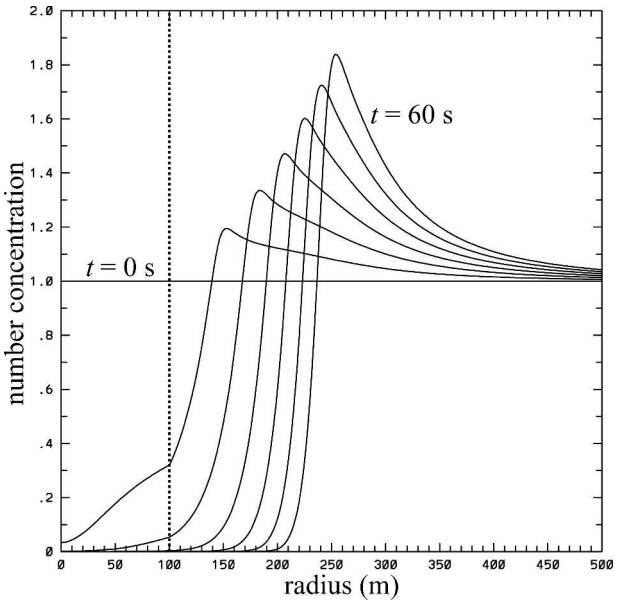

FIG. 5. Radial profiles every 10 s of the number concentration of small raindrops ($w_t = -2$ m s^{-1}) in the vortex shown in Fig. 3. The number concentration is initially uniform.

tude greater than what are considered typical Doppler velocity measurement errors (a few meters per second; Doviak et al. 1976).

The overestimation of the radial velocity indicates that a tornado will appear, on average, anomalously divergent on radar. Therefore, the lack of a strong low-level convergence signature in radar observations of tornadoes (Wurman et al. 1996; Wurman and Gill 2000; Bluestein et al. 2003) could be explained to some degree by centrifuging.

3. Two-dimensional model

To identify additional processes that affect the motions and concentrations of hydrometeors and other objects in tornadoes, we conducted experiments with a 2D, dry, anelastic, axisymmetric version of the National Severe Storms Laboratory (NSSL) Collaborative Model for Multiscale Atmospheric Simulation (NCOMMAS; Wicker and Wilhelmson 1995; Wicker and Skamarock 2002). Similar models have been used previously to study axisymmetric aspects of tornado dynamics (e.g., Smith and Leslie 1979; Fiedler 1993). Tornado-like vortices have also been simulated in fully 3D cloud models (e.g., Wicker and Wilhelmson 1995), but the additional complexities present in these moist, 3D simulations are beyond the scope of this study. We simulated tornado-like vortices by solving the following equations in a rotating cylinder:

$$\frac{\partial u_a}{\partial t} = -u_a\frac{\partial u_a}{\partial r} - w_a\frac{\partial u_a}{\partial z} + \frac{v_a^2}{r} - \frac{1}{\rho_a}\frac{\partial p}{\partial r} + 2\Omega v_a + \nu\left[\frac{1}{r}\frac{\partial}{\partial r}\left(r\frac{\partial u_a}{\partial r}\right) + \frac{\partial^2 u_a}{\partial z^2} - \frac{u_a}{r^2}\right], \tag{15}$$

$$\frac{\partial v_a}{\partial t} = -u_a\frac{\partial v_a}{\partial r} - w_a\frac{\partial v_a}{\partial z} - \frac{u_a v_a}{r} - 2\Omega u_a + \nu\left[\frac{1}{r}\frac{\partial}{\partial r}\left(r\frac{\partial v_a}{\partial r}\right) + \frac{\partial^2 v_a}{\partial z^2} - \frac{v_a}{r^2}\right], \tag{16}$$

$$\frac{\partial w_a}{\partial t} = -u_a\frac{\partial w_a}{\partial r} - w_a\frac{\partial w_a}{\partial z} - \frac{1}{\rho_a}\frac{\partial p}{\partial z} + B + \nu\left[\frac{1}{r}\frac{\partial}{\partial r}\left(r\frac{\partial w_a}{\partial r}\right) + \frac{\partial^2 w_a}{\partial z^2}\right], \tag{17}$$

$$0 = \frac{1}{r}\frac{\partial}{\partial r}(ru_a) + \frac{\partial w_a}{\partial z}, \tag{18}$$

where Ω is the angular velocity of the rotating cylindrical domain, B is a specified forcing (analogous to buoyancy) in the vertical momentum equation only, and ν is the diffusion coefficient. The wind components u_a, v_a, and w_a in the radial, tangential, and vertical directions, respectively, are functions of r (radius), z (height), and t (time). The specified air density is constant throughout the domain; thus, the continuity Eq. (18) has a simple form. The model uses third-order Runge–Kutta time integration, third-order spatial differencing for the advection terms, and second-order spatial differencing otherwise (Wicker and Skamarock 2002) to solve finite-difference approximations of the governing equations on a staggered grid (e.g., Eskridge and Das 1976; Smith and Leslie 1979).

The methodology for simulating a tornado-like vortex in a closed, rotating cylinder is like that of Fiedler (1993). To drive the updraft and ultimately the tornado-like vortex, we specified fixed forcing (Fig. 6) in the vertical momentum equation with the following structure:

$$B(r,z) = B_0\cos\left(\frac{\pi r}{2r_B}\right)\sin\left[\frac{\pi(z-z_b)}{z_t - z_b}\right], r \le r_B \quad \text{and} \quad z_b \le z \le z_t; \quad B = 0 \quad \text{otherwise}; \tag{19}$$

where B_0 is the maximum buoyancy, r_B is the radius of the forcing region, and z_b and z_t are the lower and upper heights of the forcing region, respectively. Along the axis of the cylinder, the distribution of B is associated with convective available potential energy

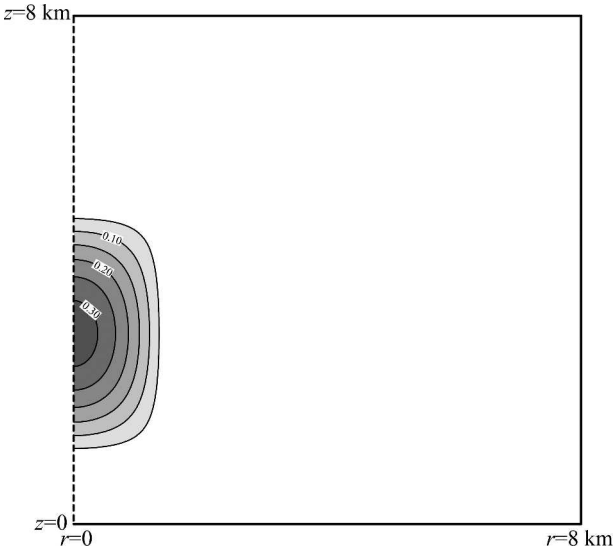

FIG. 6. Model domain used for the 2D axisymmetric simulations. The axis of the cylindrical domain is marked with a dotted line. The bottom, top, and lateral sides are rigid, no-slip boundaries. The specified forcing (B) in the vertical momentum equation (contours and shading at intervals of 0.05 m s^{-2}) in the first 2D simulation (Fig. 7) is also shown.

(CAPE) of $2B_0(z_t - z_b)/\pi$. The top, bottom, and lateral sides of the domain are rigid, no-slip boundaries, and we initialize the simulations with solid-body rotation of magnitude Ω.

We selected two simulations for detailed analysis (Figs. 7 and 8). In each simulation, the domain had a diameter of 16 km and was 8 km tall (Fig. 6). The governing equations were solved with a time step of 0.1 s on a uniform ($\Delta r = \Delta z$ 20 m) Cartesian grid. The following other parameters were common to both simulations: $\nu = 20$ m^2 s^{-1}, $\rho_a = 1.16$ kg m^{-3}, $r_B = 1500$ m, $z_b = 1000$ m, and $z_t = 5000$ m. We wanted to produce strong low-level vortices while keeping the overall rate of overturning in the domain relatively low. After some experimentation, we chose a B distribution (Fig. 6) that has a maximum in the lower half of the domain and is associated with relatively small CAPE because the forcing layer is shallow. Although the source of angular momentum in our idealized simulation is different than in 3D simulations of supercells, our results are nevertheless analogous to those of McCaul and Weisman (2001), who demonstrated that strong low-level vortices can be produced in a small-CAPE regime when the buoyancy is concentrated at low levels.

In "simulation 1" (Fig. 7), the domain's rotation rate was $\Omega = 0.0025$ s^{-1}. The maximum "buoyancy" was $B_0 = 0.33$ m s^{-2} (Fig. 6); thus, the CAPE at the center of the domain was 830 J kg^{-1}. By $t = 1200$ s in the simulation, a strong, narrow vortex with a very strong central low-level updraft (i.e., a "one cell" vortex; Davies-Jones 1986) had formed (Fig. 7). The snapshot at 1200 s represents a transient stage in the life cycle of the vortex (Fiedler and Rotunno 1986; Fiedler 1993) during which the maximum low-level wind speeds occur. Maximum speeds of radial inflow, tangential motion, and upward motion at this time were 41, 83, and 144 m s^{-1}, respectively, and all of these maxima occurred in the lowest 150 AGL. The maximum wind speeds are associated with an end-wall vortex near the surface, which permits the local flow to greatly exceed the "thermodynamic speed limit" associated with the specified buoyancy (Fiedler 1993). At later times, which will not be discussed further, the peak tangential speeds decreased and a central downdraft developed downward to low levels.

For "simulation 2" (Fig. 8), we quadrupled the rotation rate of the cylinder ($\Omega = 0.0100$ s^{-1}) and doubled the magnitude of the forcing for upward motion ($B_0 = 0.65$ m s^{-2}; 1660 J kg^{-1} maximum CAPE) relative to simulation 1. In simulation 2, the most intense stage of the vortex was followed by the formation of a strong central downdraft (not shown). Later, the central downdraft weakened. The snapshot at $t = 880$ s (Fig. 8) represents a steadier phase in the vortex life cycle. At this time, the vortex was relatively broad (the maxima in tangential and vertical velocity were near radius 500 m) and contained a much weaker low-level updraft than in simulation 1. We consider the simulation to be representative of a two-celled vortex (Davies-Jones 1986) because the maxima in vertical velocity and vertical vorticity at low levels were far from the center. However, the interior vertical-velocity structure was atypical of two-celled vortices. Whereas a two-celled vortex is typically defined as having only downdraft in the core at low levels, simulation 2 produced a weak central updraft surrounded by a weak downdraft in the core [Fig. 8c; also Fig. 6 of Fiedler (1993)].

The following equations governing object motion and number concentration were integrated in parallel with the vortex simulation:

$$\frac{\partial u_p}{\partial t} = -u_p \frac{\partial u_p}{\partial r} - w_p \frac{\partial u_p}{\partial z} + \frac{v_p^2}{r} + 2\Omega v_p + \frac{g(u_a - u_p)|\mathbf{v}_a - \mathbf{v}_p|}{w_t^2}, \tag{20}$$

$$\frac{\partial v_p}{\partial t} = -u_p \frac{\partial v_p}{\partial r} - w_p \frac{\partial v_p}{\partial z} - \frac{u_p v_p}{r} - 2\Omega u_p + \frac{g(v_a - v_p)|\mathbf{v}_a - \mathbf{v}_p|}{w_t^2}, \tag{21}$$

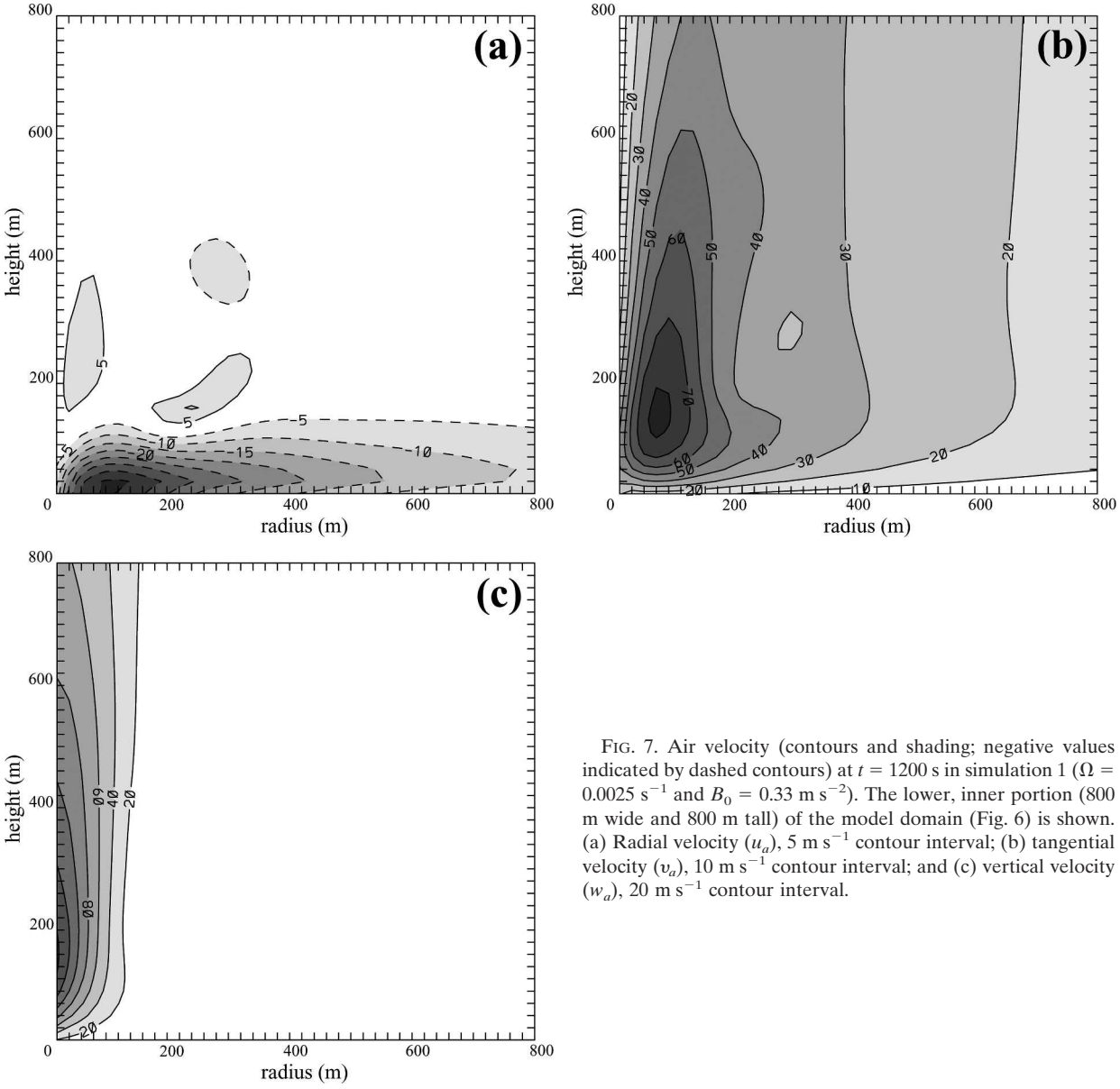

FIG. 7. Air velocity (contours and shading; negative values indicated by dashed contours) at $t = 1200$ s in simulation 1 ($\Omega = 0.0025\ \mathrm{s}^{-1}$ and $B_0 = 0.33\ \mathrm{m\ s}^{-2}$). The lower, inner portion (800 m wide and 800 m tall) of the model domain (Fig. 6) is shown. (a) Radial velocity (u_a), 5 m s^{-1} contour interval; (b) tangential velocity (v_a), 10 m s^{-1} contour interval; and (c) vertical velocity (w_a), 20 m s^{-1} contour interval.

$$\frac{\partial w_p}{\partial t} = -u_p \frac{\partial w_p}{\partial r} - w_p \frac{\partial w_p}{\partial z} - g + \frac{g(w_a - w_p)|\mathbf{v}_a - \mathbf{v}_p|}{w_t^2}, \tag{22}$$

$$\frac{\partial n}{\partial t} = -\frac{nu_p}{r} - \frac{\partial}{\partial r}(nu_p) - \frac{\partial}{\partial z}(nw_p), \tag{23}$$

where $|\mathbf{v}_a - \mathbf{v}_p| = \sqrt{(u_a - u_p)^2 + (v_a - v_p)^2 + (w_a - w_p)^2}$. As supported by the scale analysis in the previous section, the pressure-gradient terms have been neglected since we are considering hydrometeors and other objects that are much denser than air. The method for solving (20)–(23) is like that used for solving (15)–(18), except that the boundary conditions must account for objects entering and exiting the domain. We specified $w_p = w_t$ at the top and bottom boundaries of the domain and kept the number concentration fixed at the top boundary. We initialized the simulations of hydrometeors as follows: $u_p = u_a = 0$, $v_p = v_a = 0$, $w_a = 0$, $w_p = w_t$, and $n = 1.0$.

Many characteristics of the fields aloft in the 2D simulations can be explained by the 1D centrifuging process described previously. For example, in simulation 1, the maximum tangential velocity of 83 m s^{-1} occurs at radius 80 m (Fig. 7b). Equations (12)–(14) would thus predict that small raindrops ($w_t = -2$

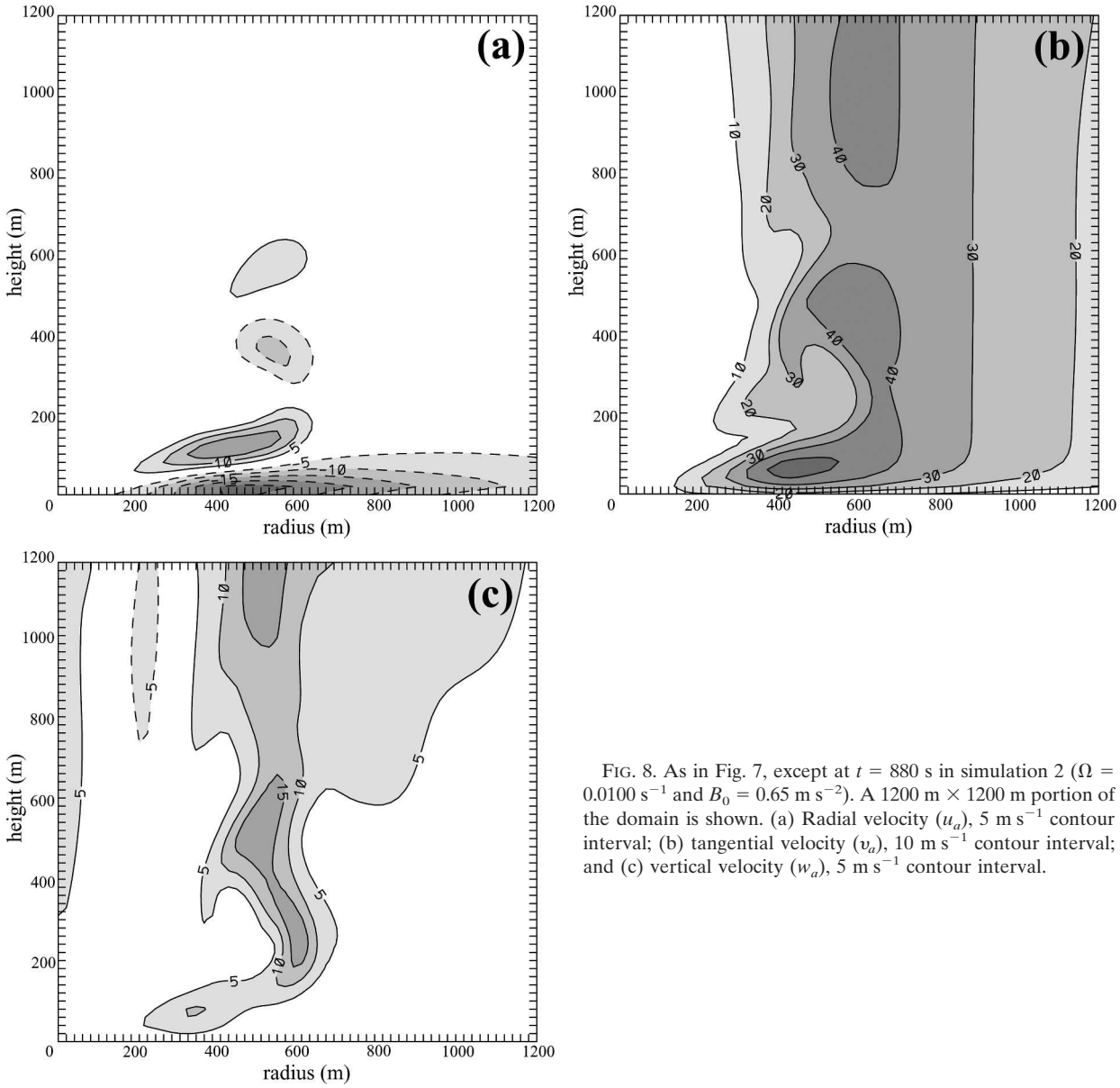

FIG. 8. As in Fig. 7, except at $t = 880$ s in simulation 2 ($\Omega = 0.0100\ \mathrm{s}^{-1}$ and $B_0 = 0.65\ \mathrm{m\ s}^{-2}$). A 1200 m $\times$ 1200 m portion of the domain is shown. (a) Radial velocity (u_a), 5 m s^{-1} contour interval; (b) tangential velocity (v_a), 10 m s^{-1} contour interval; and (c) vertical velocity (w_a), 5 m s^{-1} contour interval.

m s^{-1}) would move outward at 6 m s^{-1} relative to the air, as is indicated in the 2D simulation (Fig. 9a).

The focus here is on new issues illustrated by the 2D simulations. As would be expected, differences between air motion and object motion develop when the objects move along strong gradients in air velocity. One noteworthy region of strong gradients is near the surface, where the tangential velocities decrease downward (Figs. 7b and 8b) and there is a shallow layer of strong radial inflow (Figs. 7a and 8a). Objects falling into the layer where v_a decreases rapidly toward the surface (e.g., Fig. 10b) carry relatively larger v_p from aloft. Since it takes a finite amount of time for the drag force to slow the objects down, a shallow layer where v_p exceeds v_a develops near the surface, particularly for large, rapidly falling objects (Fig. 9d).

Similarly, objects falling into the surface-layer inflow carry relatively larger u_p. A region of positive ($u_p - u_a$) occurs where the falling objects enter the region of maximum inflow (e.g., along dashed line in Fig. 9c). This effect is more pronounced for objects with larger terminal fall speeds (Figs. 9a and 9c). In the introduction, we mentioned that strongly convergent surface layers in tornadoes are usually not observed by Doppler radars. In section 2, we noted that the 1D centrifuging process could explain some of the apparent anomalous divergence. The surface-layer-inflow effect described here provides an additional explanation for the

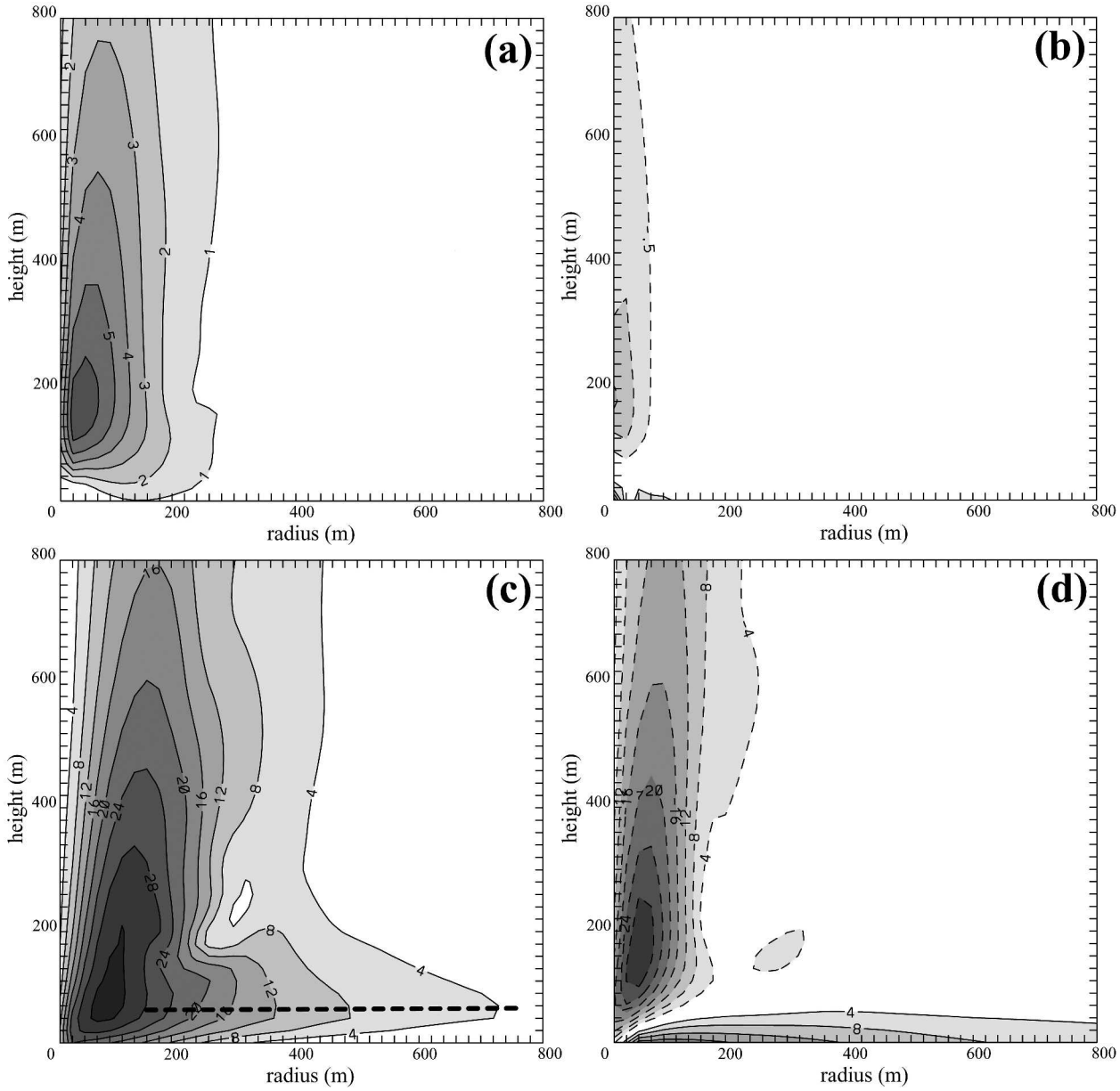

FIG. 9. Differences between object motion and air motion (contours and shading; negative values indicated by dashed contours) at $t = 1200$ s in simulation 1 (Fig. 7). (a) Radial-velocity difference ($u_p - u_a$) (1 m s^{-1} contour interval) for small raindrops ($w_t = -2$ m s^{-1}). (b) Tangential velocity difference ($v_p - v_a$) (0.5 m s^{-1} contour interval) for small raindrops ($w_t = -2$ m s^{-1}). (c) Radial-velocity difference ($u_p - u_a$) (4 m s^{-1} contour interval) for large hailstones/plywood sheets ($w_t = -20$ m s^{-1}). (d) Tangential velocity difference ($v_p - v_a$) (4 m s^{-1} contour interval) for large hailstones/plywood sheets ($w_t = -20$ m s^{-1}).

lack of convergence in the radar observations. A third possibility is that inflow layers in tornadoes are extremely shallow. In simulation 1, the inflow layer was about 100 m deep, and the fastest inflow was at 20–40 m AGL (Fig. 7a). In a large-eddy simulation by Lewellen (1993), the depth of the near-surface inflow layer was also approximately 100 m AGL. Wurman et al. (1996) noted that inflow layers in real tornadoes might be even shallower; therefore, it is difficult to resolve the details of the surface layer even with mobile radars at close range.

The remainder of this section focuses on object number concentration. The centrifuging process illustrated by the 1D model—that is, the tendency to produce relatively low number concentrations inside the vortex core and relatively high number concentrations outside the

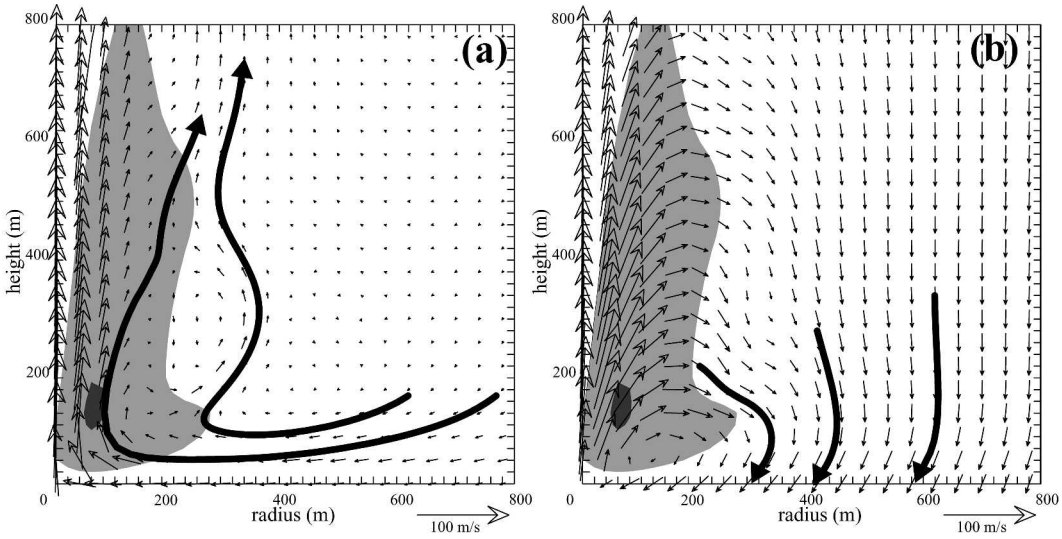

FIG. 10. Object motions in the r–z plane at $t = 1200$ s in simulation 1. Air tangential velocity (shading in regions exceeding 40 and 80 m s^{-1}; cf. Fig. 7) is also indicated. (a) Vectors and streamlines indicate the motion of small raindrops ($w_t = -2$ m s^{-1}). (b) Vectors and streamlines indicate the motion of large hailstones/plywood sheets ($w_t = -20$ m s^{-1}).

core (Fig. 5)—is still evident in the 2D simulations (Fig. 11). Centrifuging is a process associated not only with vertical vorticity but also with horizontal vorticity. For example, the relative minimum in number concentration near $r = 270$ m, $z = 290$ m in simulation 1 (indicated by the arrow in Fig. 11a) is associated with a relative maximum in horizontal vorticity (we infer loosely from the vector pattern in Fig. 10a that there is a vertical circulation associated with horizontal vorticity directed out of the page).

Perhaps the most important new effect illustrated by the 2D simulations is related to the surface-layer inflow (Figs. 7a and 8a). Negative values of u_p in the inflow layer are associated with positive values of the $-(nu_p/r)$ term in (23). Physically, number concentration increases as rings of objects contract toward the center. In the small-raindrop simulation (Fig. 10a), some raindrop trajectories that originate a few hundred meters outside the vortex core do enter the core near the surface. Along these inflow trajectories, number concentrations develop that are an order of magnitude greater than the initial concentration (Fig. 11a). [The base 10 logarithm of number concentration is plotted in Fig. 11, for easy comparison to logarithmic radar scales such as dBZ and dBm (e.g., Fig. 1c).] The greatest raindrop concentration develops just inside the radius of maximum tangential wind near the surface. A "recycling" process occurs, in which some raindrops fall into the inflow layer, are carried toward the center, and then are lifted by the updraft (Fig. 10a). As the raindrops are lifted, they are also centrifuged outward; thus, the width of the tube of maximum number concentration increases with height (Fig. 11a). The vortex core aloft is relatively free of raindrops. The raindrop distribution is reminiscent of reflectivity/power distributions in tornadoes (e.g., Fig. 1c), as summarized in the introduction.

The distribution of large hailstones evolves differently. Most importantly, no recycling of large objects occurs in simulation 1 (Fig. 10b); instead, objects outside the vortex core remain outside and eventually fall out. Those objects that are initially in the core are quickly ejected out of the core. After roughly $t = 900$ s, when the low-level vortex is developing rapidly and has reached approximately half its peak strength (not shown), the only significant concentrations of objects at low levels are several core radii away from the center (Fig. 11b).

In a tornado with a structure like that in simulation 1, large, dense objects can have significant concentrations near the core for periods of a few minutes or more only if a source of new objects exists in the core. To determine how a debris signature might appear on radar, we designed a new simulation that included a source term in the number-concentration equation: $(\partial n/\partial t) = \ldots + S$. In our simulation, we specified $S = 1.0$ s^{-1} at grid points in the lowest two model levels where the horizontal wind speed exceeded 50 m s^{-1}, and $S = 0$ otherwise. In simulation 1, the conditions necessary to activate the debris source were first produced at $t = 1080$ s. We initialized these simulations with $n = 0$ everywhere, otherwise the initialization method was like that of the hydrometeor simulations discussed previously.

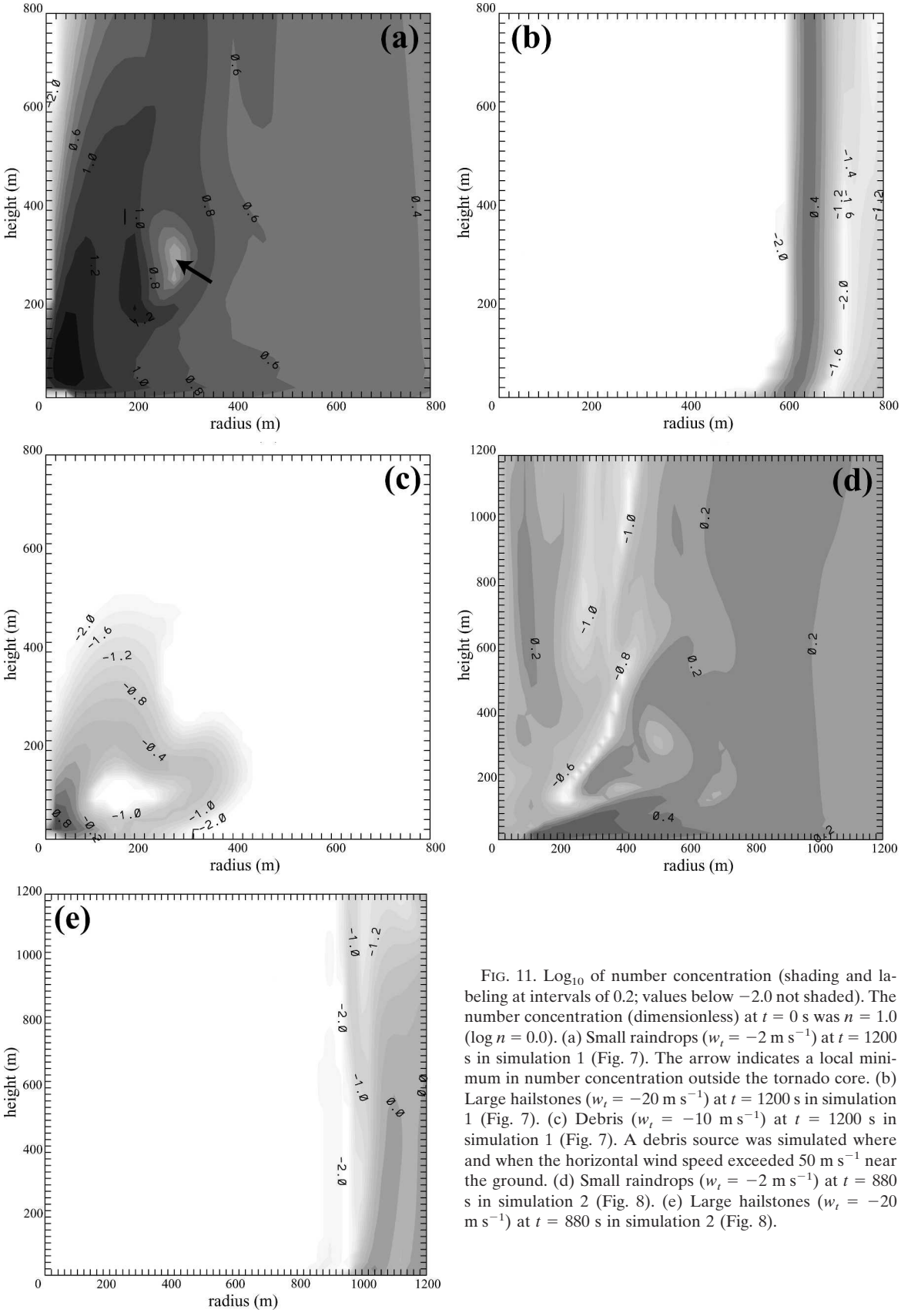

FIG. 11. Log_{10} of number concentration (shading and labeling at intervals of 0.2; values below −2.0 not shaded). The number concentration (dimensionless) at $t = 0$ s was $n = 1.0$ ($\log n = 0.0$). (a) Small raindrops ($w_t = -2$ m s^{-1}) at $t = 1200$ s in simulation 1 (Fig. 7). The arrow indicates a local minimum in number concentration outside the tornado core. (b) Large hailstones ($w_t = -20$ m s^{-1}) at $t = 1200$ s in simulation 1 (Fig. 7). (c) Debris ($w_t = -10$ m s^{-1}) at $t = 1200$ s in simulation 1 (Fig. 7). A debris source was simulated where and when the horizontal wind speed exceeded 50 m s^{-1} near the ground. (d) Small raindrops ($w_t = -2$ m s^{-1}) at $t = 880$ s in simulation 2 (Fig. 8). (e) Large hailstones ($w_t = -20$ m s^{-1}) at $t = 880$ s in simulation 2 (Fig. 8).

FIG. 12. Photograph (copyright D. Dowell) of a tornado near Fulton, SD, at 0108 UTC 31 May 1998. The arrow marks a curl in the debris cloud.

The debris fall speed in our simulation was 10 m s^{-1}, which could represent large gravel or small boards. Since the parameter choices in the debris simulation are rather arbitrary, our focus is on only the gross properties of the debris field.

In the debris simulation, a maximum in number concentration develops near the surface close to the center of the vortex (Fig. 11c). The debris pattern in the model could be related to transient inner arcs or rings of high reflectivity observed near the surface in some tornadoes (Wurman and Gill 2000). The debris cloud in the simulation expands outward with height as objects are simultaneously lifted and centrifuged. At the level where debris exits the updraft, the debris cloud curls abruptly downward. Similar curls in debris clouds are observed in some tornadoes (e.g., Fig. 12). The debris pattern in our simulation is distinctively narrow because the object sizes are uniform; such patterns would be less obvious in other cases in which debris sizes are more varied. Large objects do not reach great heights in simulation 1 because they are ejected so quickly from the updraft. For example, when the fall speed is 10–20 m s^{-1}, the maximum in debris concentration exits the updraft at around 200 m AGL (Fig. 11c). In the cross section in Fig. 11c, the complete loop is an indication of recycling. In simulation 1, 10 m s^{-1} is approximately the maximum fall speed that is associated with recycling.

Patterns in the small-raindrop concentration in simulation 2 are more complicated than in simulation 1. First, a secondary maximum in raindrop concentration is found within the tornado core's "eye" in simulation 2 (approximately along $r = 100$ m in Fig. 11d), whereas in simulation 1, the core aloft was relatively free of raindrops (Fig. 11a). As mentioned previously, a strong downdraft developed in the vortex core in simulation 2; some raindrops that were inside the core of the developing vortex at a few kilometers AGL were carried downward by this downdraft (not shown). The concentration of these raindrops that descended in the downdraft was still relatively high in the core at $t = 880$ s (Fig. 11d). The raindrop number-concentration pattern in simulation 2 reminds us of radar observations of the 3 May 1999 Mulhall, Oklahoma, tornado, in which horizontal cross sections showed relatively high reflectivity within the core (Wurman 2002), rather than the more typical low reflectivity throughout the core aloft. The Mulhall tornado was an unusually large two-celled vortex. We speculate that high reflectivity in the vortex core at a few hundred meters AGL, owing its existence to scatterers that have descended from a few kilometers AGL in the central downdraft, could be a common radar signature of two-celled vortices.

Second, although the region of concentrated raindrops near the radius of maximum tangential wind in

simulation 2 (Fig. 8b) generally expands outward with height, the maximum in concentration has significant small-scale structure (Fig. 11d). The secondary circulation, particularly the alternating pattern with height of radial inflow and outflow (Fig. 8a), appears to be a major factor in organizing the complex pattern in the concentration field. We recall the reflectivity structure of the 5 May 2002 Happy, Texas, tornado (Bluestein et al. 2004b), in which the reflectivity minimum near the surface was pear shaped. We speculate that the vertical profile of radial motion, which included elevated inflow at 200–400 m AGL, was also a major organizing factor in that case.

Other conclusions drawn from number-concentration patterns in simulation 2 are qualitatively similar to those from simulation 1. Recycling of small raindrops occurs in both simulations. In simulation 2, the highest small-raindrop concentrations (Fig. 11d) develop inside the radius of maximum tangential wind near the surface (Fig. 8b). In simulations of larger objects, no recycling occurs, and the tube of relatively high number concentration develops well outside the core (Fig. 11e).

Evidence in these simulations could indicate that objects with fall speeds of less than 10 m s^{-1}, such as small and medium raindrops, are the dominant radar scatterers in and near tornado cores aloft (i.e., above a few hundred meters AGL). (Consideration of the sixth-power relationship between returned power and drop diameter might lead one to favor the medium raindrops as the dominant scatterers.) In these simulations, larger objects were not recycled and were centrifuged quickly away from the core. These results could be interpreted as "good news" because Doppler measurement errors are less for objects that have fall speeds of less than 10 m s^{-1} than for hail and large debris.

Near the surface, small and medium raindrops might also be the dominant radar scatterers in and near the vortex core if no significant debris is being lofted. A caveat is that sub-tornado-scale features such as multiple vortices, which were not modeled in this study, could act to keep larger objects closer to the center by ejecting them into the core. If a tornado is lofting large debris, Doppler measurement errors near the surface become quite large. To correct the measurements, one must know the characteristics of the radar scatterers.

4. Observations of the Spencer, South Dakota, tornado

A Doppler On Wheels (DOW) 3-cm radar (Wurman et al. 1997; Wurman 2001) observed a large, violent tornado at ranges between 1.7 and 8.0 km in the Spencer, South Dakota, area between 0134 and 0145 UTC 31 May 1998 (Alexander and Wurman 2005). During the 11-min observing period, the tornado moved from open, rural terrain into a small (less than 1 km^2) but densely populated town, then back into open country. The tornado, which produced significant and widespread damage in the southern portion of Spencer, received an F4 damage rating (USDOC 1998).

The DOW collected volumetric observations every 40–50 s with a minimum of 6–10 samples across the tornado core (Alexander and Wurman 2005); the sample volumes were as small as $(30\ m)^3$. Doppler analyses close to the surface are possible because the beam centerlines were as low as 20–50 m AGL. The Spencer tornado was associated with the reflectivity/power signature described in section 1 (Figs. 1a, 1c, and 1e). The relative maxima in returned power came from near the edges of the visible funnel (Fig. 1e), which was composed of cloud, dust, and debris.

The analysis here focuses on relative changes in the DOW returned power[2] between 0137:42 and 0140:17 UTC (Fig. 13), when the range to the tornado increased from 3.2 to 5.1 km. At 0137:42 UTC, just prior to the tornado entering Spencer, the returned power field reveals a saturated disk of −48 dBm approximately 500 m in diameter at 30 m AGL (Fig. 13a). Less than a minute later, as the tornado was entering Spencer, the areal coverage of saturated returns in the tornado was less (Fig. 13b). The increasing range to the tornado could be the primary explanation for the decrease in returned power.

The DOW scan at 0139:30 UTC (Fig. 13c), which was collected after the tornado core had been in Spencer for approximately 1 min, indicates a dramatic increase in the area covered by saturated power returns, at odds with the expected decrease in power with increasing range. Filling of the vortex with debris as the tornado passed through Spencer could explain the increase in power. While the radiation-scattering properties of large debris are complex, the returned energy from larger scatterers in a radar volume generally provides a proportionally larger contribution to the Doppler velocity measurement than do smaller scatterers. Later in the section, we test a hypothesis that the mean scatterer

[2] We analyze the returned power rather than the reflectivity factor because the latter cannot be computed unambiguously for the following reasons: (a) the DOW radar was not calibrated relative to other radar systems such as the Weather Surveillance Radar-1988 Doppler (WSR-88D), (b) the returned power often exceeded the −48 dBm threshold of receiver saturation, and (c) some scattering in the tornado and surrounding hook echo was likely due to objects that have complex scattering properties in the Mie range because they were as large as, or larger than, the radar wavelength.

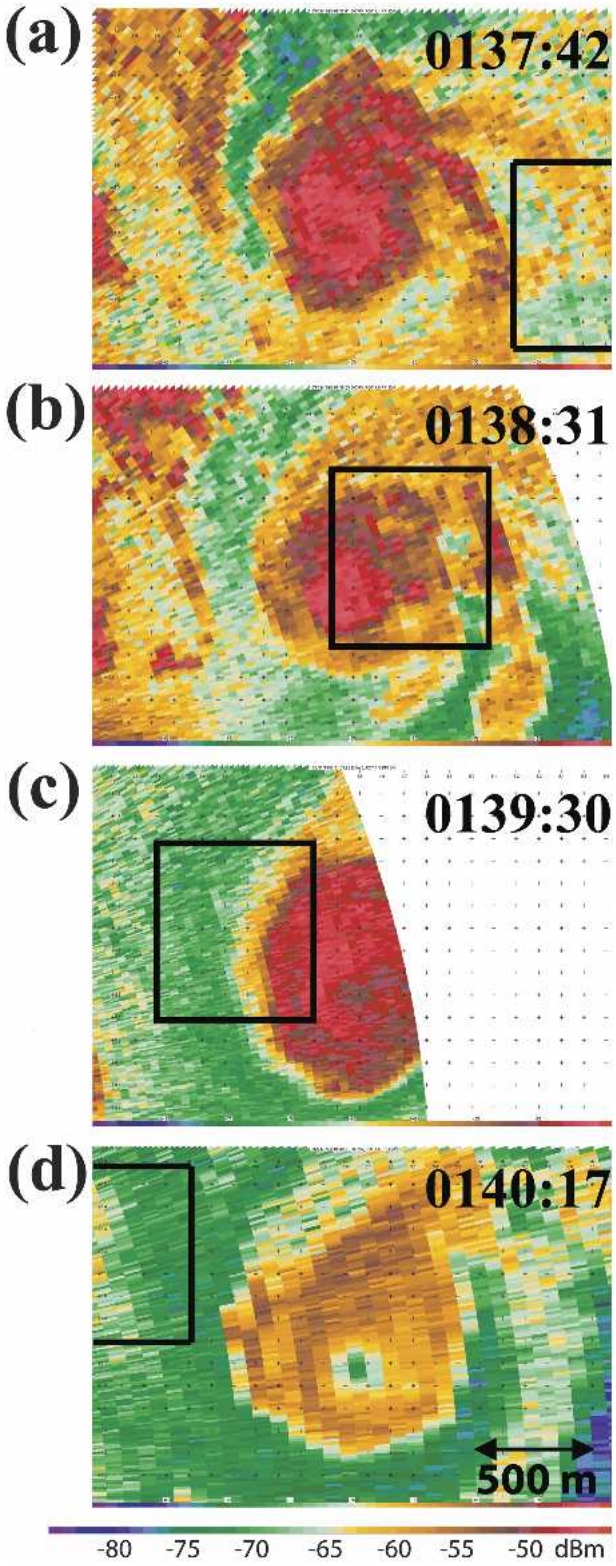

FIG. 13. DOW 1.5° elevation scan of received power (dBm) at (a) 0137:42, (b) 0138:31, (c) 0139:30, and (d) 0140:17 UTC. The scan height at the tornado center is approximately 100 m AGL. The rectangle indicates the location of Spencer, SD.

size increased as the Spencer tornado entered town and started lofting debris.

Immediately after the tornado exited Spencer, the power in the disk decreased approximately 12 dBm (Figs. 13c and 13d). At 0140:17 UTC, the disk was unsaturated with average power returns around –60 dBm (Fig. 13d); a central "eye" also became distinct with a minimum power value of –75 dBm at the tornado center. Since increasing range to the tornado would have accounted for only a 1.0-dBm decrease in returned power between 0139:30 and 0140:17 UTC, it appears that a significant change in scatterer type and/or concentration was responsible for the observed 12-dBm decrease. We propose that after the tornado exited Spencer, the larger debris was quickly ejected from the core and fell out (section 3). If we assume that the debris had a fall speed of over 10 m s^{-1} and reached heights of several hundreds of meters or less, then much of the debris would have fallen out within several tens of seconds after the tornado exited Spencer. We dismiss a change in radar parameters (made obvious by the longer gate length in Fig. 13d) as an explanation for the large power decreases in the tornado because returned power from the surrounding clear-air region decreased only about 3 dBm between the times corresponding to Figs. 13c and 13d.

According to the model results (sections 2 and 3), an abrupt change in scatterer type (e.g., from raindrops to large debris) in a quasi-steady tornado would be associated with an abrupt change in the Doppler velocity signature. Therefore, we examined in detail the Doppler measurements of the Spencer tornado during the period when the tornado entered town and started lofting debris. To facilitate the study of the Spencer tornado, we retrieved profiles of the radial and tangential components of scatterer motion from the Doppler observations. Our retrieval method differs from the ground-based velocity track display technique (Lee et al. 1999) applied by Bluestein et al. (2003) and Lee and Wurman (2005) to other tornado datasets in that our method does not require data interpolation, uses an a priori estimate of tornado motion (described below) rather than retrieving it, treats the background flow as a known quantity (equal to tornado motion), and only aims to retrieve the azimuthally averaged (zero wavenumber) components. Axisymmetric profiles $u_p(r)$ and $v_p(r)$ that fit the Doppler data in a least squares sense were retrieved by finding minima in the following cost function within annuli surrounding the tornado center:

$$J = \sum_i [D_i - u_p \cos(\alpha_i - \theta_i) - v_p \sin(\alpha_i - \theta_i) - C \cos(\beta - \theta_i)]^2, \quad (24)$$

where the index i refers to a particular observation within the annulus; D_i is the Doppler velocity; α_i and θ_i are the azimuth angles of the observation with respect to the tornado center and radar, respectively; C is the tornado's translational speed; and β is the direction of tornado motion. The tornado-motion estimates are based upon locations of the Doppler-velocity couplet center in consecutive radar scans at the same elevation angle.

The following solution for the unknowns u_p and v_p can be obtained from the Euler–Lagrange equations derived from (24):

$$u_p(r) = \frac{\sum_i a_i^2 \sum_i b_i c_i - \sum_i a_i b_i \sum_i a_i c_i}{\sum_i a_i^2 \sum_i b_i^2 - \left(\sum_i a_i b_i\right)^2}, \quad (25)$$

$$v_p(r) = \frac{\sum_i b_i^2 \sum_i a_i c_i - \sum_i a_i b_i \sum_i b_i c_i}{\sum_i a_i^2 \sum_i b_i^2 - \left(\sum_i a_i b_i\right)^2}, \quad (26)$$

where

$$a_i = \sin(\alpha_i - \theta_i), \quad b_i = \cos(\alpha_i - \theta_i), \quad \text{and}$$
$$c_i = D_i - C\cos(\beta - \theta_i). \quad (27)$$

From Doppler data at approximately 0.5° elevation angle in each of several volumes, we obtained velocity profiles by solving (25) and (26) in 40-m-wide annuli, at 20-m intervals, from near the tornado center to outside the core. This technique employs no assumption about the vortex profiles other than axisymmetry.

The raw Doppler data (Fig. 14) and the retrieved profiles of tangential motion (Fig. 15a) indicate that over the observation period, the tornado core was apparently getting wider and the peak tangential velocities were apparently decreasing. One interpretation of the trends is that the tornado was actually evolving significantly. A second interpretation is that these changes in the Doppler velocity field resulted from a change in mean scatterer size; that is, the 1D modeling results (section 2) indicate that an increase in scatterer size (fall speed) would be associated with a decrease in the maximum tangential Doppler velocity and an increase in the radius where the maximum is located. Since the observations indicate that the tornado core was already getting wider before the tornado entered Spencer (Alexander and Wurman 2005), actual tornado evolution is probably the primary explanation for the trends in the tangential Doppler velocities.

However, some influence on the Doppler measurements by centrifuging is indicated by the analysis of

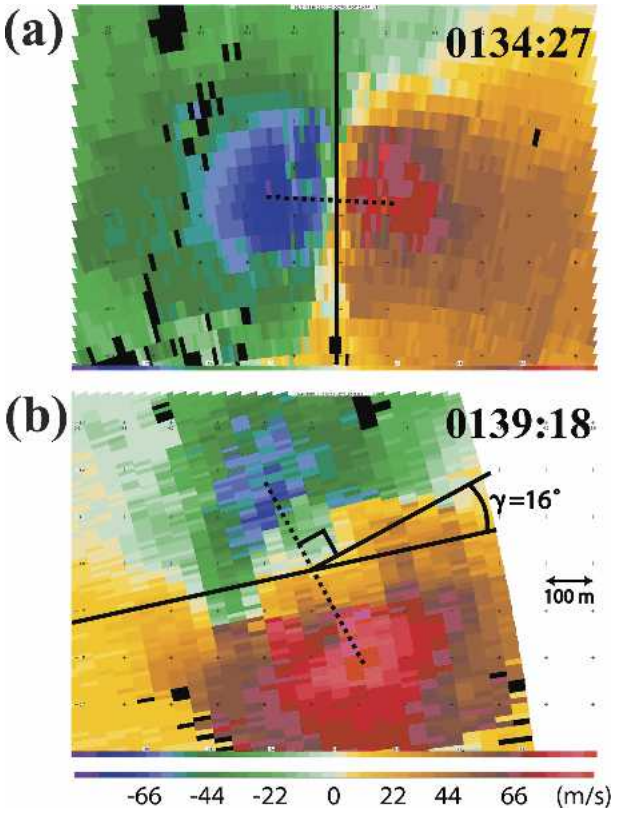

FIG. 14. DOW3 Doppler velocity (m s^{-1}) at 0.5° elevation angle at (a) 0134:27 UTC, representing the closest approach of the tornado to the radar during the observing period, and (b) 0139:18 UTC, when the tornado was in Spencer, SD. The scan height at the center of the tornado is approximately 20 and 40 m AGL in (a) and (b), respectively. The range to the tornado is 1.7 and 4.4 km in (a) and (b), respectively. The radar-viewing direction through the center of the tornado is indicated by a solid black line. The dashed line connects the centers of the inbound and outbound velocity anomalies.

Wurman and Alexander (2005), who carefully determined the earth-relative observation locations (Alexander and Wurman 2005) and then constructed a detailed map of the estimated maximum low-level wind speeds throughout the Spencer area (not shown). According to their analysis, the axis of maximum radar-estimated wind speeds is parallel to, but is displaced approximately 50 m to the right (south) of, the axis of most severe (F4) damage. The displacement between the axes of maximum radar-estimated wind speeds and most severe damage appears to be a persistent feature across Spencer and could provide evidence of errors associated with equating scatterer motion to air motion. The core width and peak tangential velocity in the Spencer tornado (Fig. 15a) are comparable to those in the idealized 1D model experiments with $V = 100$ m s^{-1} and $R = 200$ m (rows 5–6 in Table 2). In the

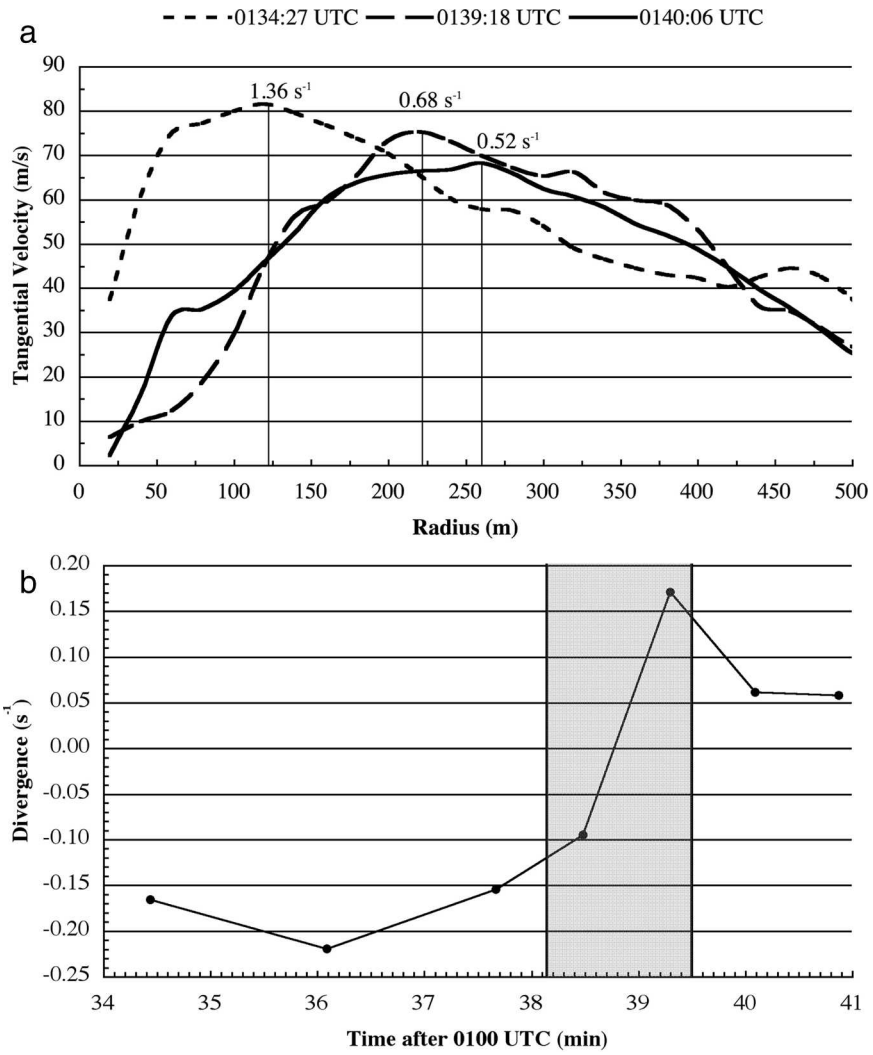

FIG. 15. Retrieved axisymmetric Doppler velocities at 0.5° elevation angle (approximately 30 m AGL). (a) Tangential velocity (m s^{-1}) as a function of radius (m) at 0134:27 UTC, when the tornado was closest to DOW3; at 0139:18 UTC, when the tornado was in Spencer, SD; and at 0140:06 UTC, when the tornado was just southeast of Spencer. Mean vertical vorticity (s^{-1}) in the tornado core is also indicated. Vertical lines indicate the radii of maximum tangential velocities. (b) Mean horizontal divergence (s^{-1}) in the tornado core [$2u_p(R)/R$, where R is the radius of maximum tangential velocity] as a function of time (UTC). The gray shading indicates the time period when the tornado core was in Spencer.

model, the displacements of the maxima in v_p from the maxima in v_a were 20–120 m for the plywood sheets and bricks; the observed 50-m displacement lies within this range.

Perhaps the most compelling evidence for centrifuging of scatterers is in the analyses of radial scatterer motion. Profiles retrieved from the Doppler data at 0.5° elevation angle before 0139 UTC indicate horizontal convergence on average over the tornado core (Fig. 15b). Since the beam centerlines were as low as 20 m AGL, the DOW may have been sampling some of the shallow tornado inflow near the surface (e.g., Lewellen 1993). When the tornado reached Spencer, the Doppler-velocity signature changed abruptly. The orientation of the Doppler-velocity couplet changed between 0134 and 0139 UTC (Fig. 14) in a manner that would indicate a significant increase in the horizontal divergence of the scatterers (Brown and Wood 1991). Using Brown and Wood's method, we estimated the peak axisymmetric radial component at 0139 UTC (Fig. 14b) as follows: $u_p = \overline{D}\sin\gamma = (80\ \text{m s}^{-1})\sin 16° = 22\ \text{m s}^{-1}$, where $\overline{D}$ is the average of the Doppler velocity extrema

and γ is the angle between the radar-viewing direction and the perpendicular bisector of a line that connects the extrema. Since the core radius was $R = 220$m, the estimated divergence over the core at 0139 UTC was thus $(2u_p/R) = [(2)(22 \text{ m s}^{-1})/220 \text{ m}] = 0.20 \text{ s}^{-1}$.

The divergence anomaly during the tornado's passage through Spencer shows up clearly in the retrieved axisymmetric profiles; convergence of 0.10 s^{-1} at 0138:27 UTC is followed by *divergence* of even greater magnitude at 0139:18 UTC (Fig. 15b). The retrieved divergence of 0.17 s^{-1} at 0139 UTC is consistent with the magnitude inferred previously from the raw measurements. The magnitude of the divergence differences between 0138 and 0139 UTC, which is much greater than the magnitude of previous fluctuations, is associated with a 30 m s^{-1} increase in u_p near the edge of the core. Revisiting our hypothesis concerning the change in dominant scatterer type as the tornado passed through Spencer, we note that in the 1D model discussed previously (rows 5–6 in Table 2), a change in scatterer type from small raindrops to plywood sheets would have been associated with an increase in peak u_p of over 26 m s^{-1}, which is comparable to the observed increase in u_p.

The analyses indicate less low-level divergence in the core after the tornado exited Spencer (Fig. 15b). We propose that as the larger debris fell out, the size of the scatterers producing most of the returned energy gradually decreased. The decrease in scatterer size (fall speed) could explain the decrease in apparent divergence. However, since the analysis at 0140:53 UTC (roughly 1.5 min after the tornado exited Spencer) still indicates divergence rather than convergence, it is possible that some lighter debris had not yet fallen out. Another possibility is that as the tornado was moving away from the radar, each successive 0.5° scan was less able to resolve the surface-layer inflow.

5. Conclusions

We employed idealized 1D and 2D numerical models to illustrate motions and number concentrations of hydrometeors and debris within tornadoes. Aloft, where horizontal flow in the tornado is characterized mostly by rotation, objects move outward relative to the air and move more slowly than the air in the tangential direction; in addition, the vertical air-relative speed of an object is less than it is in still air. The maximum in tangential object motion occurs outside the maximum in tangential air motion. Within only a few tens of seconds, the outward motion of hydrometeors and debris decreases their number concentration within the tornado core by orders of magnitude and increases their concentration somewhat outside the core. The magnitudes of all these effects are greater for larger, denser objects, which have larger characteristic fall speeds.

Near the surface, an important tornado feature in the 2D axisymmetric simulations is the shallow layer of strong inflow. Large differences between object motion and air motion can develop as objects fall into the inflow layer. The inflow can concentrate objects and carry the objects into the updraft. This "recycling" mechanism can explain number concentrations near the tornado core that are orders of magnitude greater than in the surroundings. Furthermore, in the simulations, the ring of high number concentration generally expands with height because objects that are lifted by the updraft are also centrifuged outward; the resulting number-concentration patterns are much like the tapered or truncated cones of high reflectivity seen in high-resolution radar scans of tornadoes. In the 2D axisymmetric simulations described here, recycling occurred only for objects with fall speeds of less than 10 m s^{-1}, such as small and medium raindrops. Larger hydrometeors and debris were not recycled and were quickly centrifuged to several core radii away from the center. Based on these simulations, we speculate that the dominant scatterers observed by radar near tornado cores are generally small and medium raindrops. In tornadoes that are lofting considerable debris, the dominant scatterer at low levels might be the debris instead. In unusual cases when there is no precipitation near the tornado and the tornado is too weak to loft debris, insects could be significant scatterers.

Close-range observations by the DOW of a tornado passing from relatively open country to a small but densely populated town provided a unique opportunity to apply the theory developed from the model experiments to observations. The following changes in the observations as the tornado entered Spencer, South Dakota, are consistent with a change in scatterer type from small hydrometeors to large debris: an increase in returned power, an apparent broadening of the tornado core, a decrease in the maximum tangential Doppler velocities, a displacement between the axes of maximum Doppler velocity and of most severe damage, and a sign change in the radial-velocity component near the surface.

An important use for radar observations is to verify laboratory and numerical models of airflow in tornadoes. In the observations, differences between the air motion and the object motion are part of the measurement errors. The measurement errors depend greatly on the nature of the scatterers. With only traditional radar observations (Doppler velocity and reflectivity), one cannot distinguish between changes in scatterer

type and true changes in the wind field. Conceivably, with independent knowledge of the scatterer type, it would be possible to retrieve the air motion from the observations of object motion. A method for determining the scatterer type in tornadoes is needed. It might be feasible to determine scatterer size and shape by comparing attenuation patterns in measurements at multiple frequencies (Bluestein and Pazmany 2000) and by comparing dual-polarization measurements. Releasing scatterers (chaff) of a known type into tornadoes and comparing their motions to motions of other ambient scatterers could also be useful. An in situ method for collecting particles in tornadoes might also be possible.

A number of simplifying assumptions were employed for the numerical simulations in this study. Rather than using a drag coefficient that is specified as a constant for each object type, one could consider for future work using a drag coefficient that more realistically depends on the object-relative airspeed. Another avenue for future study of scatterer motions and concentrations in tornadoes would be to use 3D simulations. The importance of such features as multiple subvortices and asymmetries associated with tornado motion could be investigated.

Acknowledgments. This research was supported by the Advanced Study Program at the National Center for Atmospheric Research (NCAR) and by the National Science Foundation under Grants 0333872, 0437505, and 9703032. The lead author's participation in the Radar Observations of Tornadoes and Thunderstorms Experiment (ROTATE) in 1998 was supported by the National Science Foundation under Grant 9612674. The DOWs are operated by the Center for Severe Weather Research (CSWR) and have been developed by CSWR, the University of Oklahoma, NCAR's Atmospheric Technology Division (ATD), and the National Severe Storms Laboratory. Support for the DOW program has been received from the state of Oklahoma, the NSF, the Office of Naval Research, and CSWR. Rich Rotunno and two anonymous reviewers provided helpful comments on the manuscript.

REFERENCES

Alexander, C. R., and J. Wurman, 2005: The 30 May 1998 Spencer, South Dakota, storm. Part I: The structural evolution and environment of the tornadoes. *Mon. Wea. Rev.,* **133,** 72–96.

Bluestein, H. B., and A. L. Pazmany, 2000: Observations of tornadoes and other convective phenomena with a mobile 3-mm wavelength, Doppler radar: The spring 1999 field experiment. *Bull. Amer. Meteor. Soc.,* **81,** 2939–2951.

——, J. G. LaDue, H. Stein, D. Speheger, and W. P. Unruh, 1993: Doppler radar wind spectra of supercell tornadoes. *Mon. Wea. Rev.,* **121,** 2200–2221.

——, W.-C. Lee, M. Bell, C. C. Weiss, and A. L. Pazmany, 2003: Mobile Doppler radar observations of a tornado in a supercell near Bassett, Nebraska, on 5 June 1999. Part II: Tornado-vortex structure. *Mon. Wea. Rev.,* **131,** 2968–2984.

——, C. C. Weiss, and A. L. Pazmany, 2004a: Doppler radar observations of dust devils in Texas. *Mon. Wea. Rev.,* **132,** 209–224.

——, ——, and A. L. Pazmany, 2004b: The vertical structure of a tornado near Happy, Texas, on 5 May 2002: High-resolution, mobile, W-band, Doppler radar observations. *Mon. Wea. Rev.,* **132,** 2325–2337.

Bohne, A. R., 1982: Radar detection of turbulence in precipitation environments. *J. Atmos. Sci.,* **39,** 1819–1837.

Brown, R. A., and V. T. Wood, 1991: On the interpretation of single-Doppler velocity patterns within severe thunderstorms. *Wea. Forecasting,* **6,** 32–48.

Burgess, D. B., M. A. Magsig, J. Wurman, D. C. Dowell, and Y. Richardson, 2002: Radar observations of the 3 May 1999 Oklahoma City tornado. *Wea. Forecasting,* **17,** 456–471.

Davies-Jones, R. P., 1986: Tornado dynamics. *Thunderstorm Morphology and Dynamics*, E. Kessler, Ed., University of Oklahoma Press, 197–236.

——, 2000: Can the hook echo instigate tornadogenesis barotropically? Preprints, *20th Conf. on Severe Local Storms*, Orlando, FL, Amer. Meteor. Soc., 269–272.

Doviak, R. J., P. S. Ray, R. G. Strauch, and L. J. Miller, 1976: Error estimation in wind fields derived from dual-Doppler radar measurement. *J. Appl. Meteor.,* **15,** 868–878.

Dowell, D. C., and H. B. Bluestein, 2002: The 8 June 1995 McLean, Texas, storm. Part I: Observations of cyclic tornadogenesis. *Mon. Wea. Rev.,* **130,** 2626–2648.

Eskridge, R. E., and P. Das, 1976: Effect of a precipitation-driven downdraft on a rotating wind field: A possible trigger mechanism for tornadoes? *J. Atmos. Sci.,* **33,** 70–84.

Fiedler, B. H., 1989: Conditions for laminar flow in geophysical vortices. *J. Atmos. Sci.,* **46,** 252–259.

——, 1993: Numerical simulation of axisymmetric tornadogenesis in forced convection. *The Tornado: Its Structure, Dynamics, Prediction, and Hazards, Geophys. Monogr.,* No. 79, Amer. Geophys. Union, 41–48.

——, and R. Rotunno, 1986: A theory for the maximum windspeeds in tornado-like vortices. *J. Atmos. Sci.,* **43,** 2328–2340.

Fujita, T. T., 1981: Tornadoes and downbursts in the context of generalized planetary scales. *J. Atmos. Sci.,* **38,** 1511–1534.

Golden, J. H., and D. Purcell, 1977: Photogrammetric velocities for the Great Bend, Kansas, tornado of 30 August 1974: Accelerations and asymmetries. *Mon. Wea. Rev.,* **105,** 485–492.

Gunn, R., and G. D. Kinzer, 1949: The terminal velocity of fall for water droplets in stagnant air. *J. Meteor.,* **6,** 243–248.

Hoecker, W. H., 1960: Wind speed and airflow patterns in the Dallas tornado of April 2, 1957. *Mon. Wea. Rev.,* **88,** 167–180.

Kangieser, P. C., 1954: A physical explanation of the hollow structure of waterspout tubes. *Mon. Wea. Rev.,* **82,** 147–152.

Lee, W.-C., and J. Wurman, 2005: Diagnosed three-dimensional axisymmetric structure of the Mulhall tornado on 3 May 1999. *J. Atmos. Sci.,* in press.

——, B. J.-D. Jou, P.-L. Chang, and S.-M. Deng, 1999: Tropical cyclone kinematic structure retrieved from single-Doppler radar observations. Part I: Interpretation of Doppler velocity patterns and the GBVTD technique. *Mon. Wea. Rev.,* **127,** 2419–2439.

Lewellen, W. S., 1993: Tornado vortex theory. *The Tornado: Its Structure, Dynamics, Prediction, and Hazards, Geophys. Monogr.,* No. 79, Amer. Geophys. Union, 19–39.

Magsig, M. A., and J. T. Snow, 1998: Long-distance debris transport by tornadic thunderstorms. Part I: The 7 May 1995 supercell thunderstorm. *Mon. Wea. Rev.,* **126,** 1430–1449.

Marshall, T. P., 2002: Tornado damage survey at Moore, Oklahoma. *Wea. Forecasting,* **17,** 582–598.

Martin, W. J., 1998: Hail trajectories and fall speeds with rotation and wind shear. Preprints, *19th Conf. on Severe Local Storms*, Minneapolis, MN, Amer. Meteor. Soc., 64–67.

Matson, R. J., and A. W. Huggins, 1980: The direct measurement of the sizes, shapes and kinematics of falling hailstones. *J. Atmos. Sci.,* **37,** 1107–1125.

McCaul, E. W., and M. L. Weisman, 2001: The sensitivity of simulated supercell structure and intensity to variations in the shapes of environmental buoyancy and shear profiles. *Mon. Wea. Rev.,* **129,** 664–687.

Minor, J. E., K. C. Mehta, and J. R. McDonald, 1977: The tornado: An engineering oriented perspective. NOAA Tech. Memo. ERL, NSSL-82, 196 pp.

Pruppacher, H. R., and K. V. Beard, 1970: A wind tunnel investigation of the internal circulation and shape of water drops falling at terminal velocity in air. *Quart. J. Roy. Meteor. Soc.,* **96,** 247–256.

Smith, R. K., and L. M. Leslie, 1979: A numerical study of tornadogenesis in a rotating thunderstorm. *Quart. J. Roy. Meteor. Soc.,* **105,** 107–127.

Snow, J. T., 1984: On the formation of particle sheaths in columnar vortices. *J. Atmos. Sci.,* **41,** 2477–2491.

Stackpole, J. D., 1961: The effectiveness of raindrops as turbulence sensors. Preprints, *Ninth Weather Radar Conf.*, Kansas City, MO, Amer. Meteor. Soc., 212–217.

Stout, G. E., and F. A. Huff, 1953: Radar records Illinois tornadogenesis. *Bull. Amer. Meteor. Soc.,* **34,** 281–284.

USDOC, 1998: Service assessment: Spencer, South Dakota, tornado May 30, 1998. NOAA/NWS, 11 pp.

van Tassell, E. L., 1955: The North Platte Valley tornado outbreak of June 27, 1955. *Mon. Wea. Rev.,* **83,** 255–264.

Wakimoto, R. M., and B. E. Martner, 1992: Observations of a Colorado tornado. Part II: Combined photogrammetric and Doppler radar analysis. *Mon. Wea. Rev.,* **120,** 522–543.

——, W.-C. Lee, H. B. Bluestein, C.-H. Liu, and P. H. Hildebrand, 1996: ELDORA observations during VORTEX 95. *Bull. Amer. Meteor. Soc.,* **77,** 1465–1481.

Wicker, L. J., and R. B. Wilhelmson, 1995: Simulation and analysis of tornado development and decay within a three-dimensional supercell thunderstorm. *J. Atmos. Sci.,* **52,** 2675–2703.

——, and W. C. Skamarock, 2002: Time-splitting methods for elastic models using forward time schemes. *Mon. Wea. Rev.,* **130,** 2088–2097.

Wurman, J., 2001: The DOW mobile multiple-Doppler network. Preprints, *30th Int. Conf. on Radar Meteorology*, Munich, Germany, Amer. Meteor. Soc., 95–97.

——, 2002: The multiple-vortex structure of a tornado. *Wea. Forecasting,* **17,** 473–505.

——, and S. Gill, 2000: Finescale radar observations of the Dimmitt, Texas (2 June 1995), tornado. *Mon. Wea. Rev.,* **128,** 2135–2164.

——, and T. Samaras, 2004: Comparison of in-situ pressure and DOW Doppler winds in a tornado and RHI vertical slices through 4 tornadoes during 1996–2004. Preprints, *22d Conf. on Severe Local Storms*, Hyannis, MA, Amer. Meteor. Soc., CD-ROM, 15.4.

——, and C. R. Alexander, 2005: The 30 May 1998 Spencer, South Dakota, storm. Part II: Comparison of observed damage and radar-derived winds in the tornadoes. *Mon. Wea. Rev.,* **133,** 97–119.

——, J. M. Straka, and E. N. Rasmussen, 1996: Fine-scale Doppler radar observations of tornadoes. *Science,* **272,** 1774–1777.

——, M. Randall, and A. Zahrai, 1997: Design and deployment of a portable, pencil-beam, pulsed, 3-cm Doppler radar. *J. Atmos. Oceanic Technol.,* **14,** 1502–1512.

Zrnic, D. S., R. J. Doviak, and D. W. Burgess, 1977: Probing tornadoes with a pulse-Doppler radar. *Quart. J. Roy. Meteor. Soc.,* **103,** 707–720.

——, D. W. Burgess, and L. Hennington, 1985: Doppler spectra and estimated windspeed of a violent tornado. *J. Climate Appl. Meteor.,* **24,** 1068–1081.